

## Research Article

# High-Fidelity Numerical Investigation on Elucidating Sodium Heat Transfer Characteristics for 37-Pin Wire-Wrapped Fuel Bundle in the PLANDTL Facility

Giuk Choi <sup>1,2</sup>, Sujong Yoon <sup>2</sup>, Minseop Song <sup>2,3</sup> and Jae-Ho Jeong <sup>1</sup>

<sup>1</sup>Department of Mechanical Engineering, Gachon University, 1342, Seongnam-daero, Sujeong-gu, Seongnam-si, Gyeonggi-do, 13120, Republic of Korea

<sup>2</sup>Idaho National Laboratory, 2525 Fremont Avenue, Idaho Falls, ID 83415-6188, USA

<sup>3</sup>Department of Nuclear Engineering, Hanyang University, 222, Wangsimni-ro, Seongdong-gu, Seoul, Republic of Korea

Correspondence should be addressed to Minseop Song; [hysms@hanyang.ac.kr](mailto:hysms@hanyang.ac.kr) and Jae-Ho Jeong; [jaeho.jeong@gachon.ac.kr](mailto:jaeho.jeong@gachon.ac.kr)

Received 24 March 2023; Revised 13 June 2023; Accepted 5 July 2023; Published 8 August 2023

Academic Editor: Guojun Yu

Copyright © 2023 Giuk Choi et al. This is an open access article distributed under the Creative Commons Attribution License, which permits unrestricted use, distribution, and reproduction in any medium, provided the original work is properly cited.

This study involved a Reynolds-averaged Navier-Stokes- (RANS-) based computational fluid dynamics (CFD) analysis of the 37-pin wire-wrapped fuel bundle of the PNC Plant dynamics test loop (PLANDTL) facility. Previously, mainly the hydrodynamic phenomena of the wire-wrapped fuel bundle were analyzed, but the present study additionally included heat transfer analysis through conjugate heat transfer. The main purpose of the study was to benchmark the experimental data of the PLANDTL 37-pin wire-wrapped fuel bundle to investigate the heat transfer phenomena. In addition, the aim was to verify the accuracy of the RANS-based CFD analysis method using the STAR-CCM+ simulation software in comparison with the experimental data. The grid used for verification was an innovative grid system consisting of hexahedra using Fortran-based code. The development of the RANS-based CFD methodology included grid sensitivity analysis, turbulence model sensitivity analysis, and turbulent Prandtl number sensitivity analysis. Information on the temperature, mass flow rate, and area of the CFD results for each subchannel was provided for the top of the heated section and is expected to serve as a reference for future studies aiming to perform the validation and verification of a PLANDTL facility. In addition, the dependence of the peak temperature on the azimuth angle of each pin was analyzed.

## 1. Introduction

The fact that liquid metal is used as a coolant in the majority of fast reactor technologies highlights the significance of improving our knowledge of the liquid metal coolant by developing appropriate modeling methods. Liquid metal fast reactors (LMFRs) are expected to play an important role in the future of nuclear energy due to their availability, high power density, and safety resulting from the superior heat transfer properties of liquid metal. In the core of a nuclear reactor, where heat is generated in the nuclear fuel and transported to the coolant, a nuclear chain reaction occurs as the source of fission energy. The core typically consists of hundreds of nuclear fuel assemblies, each of which is made up of many fuel rods. Because the wire spacer looped

around the fuel rod prevents contact between the rods at a narrow distance and enhances the heat transfer effect, the wire spacer type is typically used for SFR core designs. It also has the effect of accelerating the mixing of the coolant. Sodium, the coolant, flows in through the inlet nozzle, receives heat from the fuel pin, rises along the wire spacer, circulates around the fuel pin, and flows out to the outlet. Although the flow phenomenon of the liquid metal, which is the coolant, is complicated by the wire spacer, the heat transfer phenomenon of the nuclear fuel assembly is very important for the design and safety analysis of such a nuclear reactor.

Since the temperature distribution determines the maximum temperature of the coolant and cladding, it is necessary to analyze the heat transfer phenomenon of the wire-

wrapped fuel bundle to evaluate the design and safety. The simulation of heat transfer in the core is crucial for the design and safety assessment of nuclear reactors. Most experimental correlations for the heat transfer behavior in liquid metals and in the fuel bundle contain large uncertainties for liquid metals. The experiment is challenging, with relatively significant experimental uncertainty and considerable cost, due to the difficulty and constraints to detect the velocity field using particle image velocimetry (PIV) and the temperature distribution of the liquid metal. Therefore, the continuous development of numerical analysis methods and computational techniques has led to the increasing use of simulation methods such as computational fluid dynamics (CFD) by reactor designers in the nuclear industry [1]. However, the methodology developed on the basis of CFD needs to be validated against experimental data first. Unfortunately, because the number of relevant experimental databases is very limited and not fully open to the public, the modeling approach related to heat transfer may be incompletely validated. In addition, since the experimental data are not designed for CFD validation, it does not contain all the information and solutions necessary for numerical analysis, and it is practically impossible to recover the missing information. In this study, we planned to collect data from a given experimental report, refine it for CFD research, and analyze it in detail. With appropriate validation of the relevant data, our work demonstrates that the CFD methodology developed and proven primarily on limited benchmark data can be successfully used for testing.

A study of the thermohydraulic phenomenon in a fuel assembly mainly involves the analysis of the pressure drop and temperature distribution of sodium during normal operation and flow phenomena at low flow rates such as natural circulation, blockage effect, and boiling effect. The temperature distribution in the fuel assembly is determined by the axial and radial power distribution in the assembly, the mass flow rate distribution for each subchannel, and the mixing effect (wire spacer effect, turbulence effect). Kabir and Hayafune analyzed the temperature distribution in the coolant using experimental data from low-flow transient sodium boiling to simulate loss-of-flow (LOF) events at the PLANDTL facility [2]. In addition, the predictive ability of the super system code (SSC) and subassembly boiling evolution analysis (SABENA) codes were analyzed using the radial temperature distribution and boiling test data [2]. The PLANDTL facility is described in detail in the following section. The LOF transient test was performed at the PLANDTL facility to accumulate thermal-hydraulic experimental data of the fuel assembly by simulating the loss-of-piping-integrity (LOPI) event at MONJU. In parallel with the experiment, the code analysis of SSC and SABENA was also validated by analyzing the LOPI transient experiments. In later follow-up experiments, the validated SSC and SABENA codes were used to examine the LOPI transients in the MONJU reactor. The simulation of the LOPI event led to the prediction that sodium boiling would occur in a part of the fuel assembly even if the power conditions approximated the rated power.

In this study, RANS-based CFD calculations were performed the STAR-CCM+ simulation software to verify its ability to predict the heat transfer phenomena of the fuel assembly using the thermal data of the 37-pin wire-wrapped fuel bundle of the PLANDTL facility. This CFD methodology is based on the innovative grid system developed in previous studies using Song's work on the experiment [3–5], and it is implemented with a Menter's shear stress transport (SST) turbulence model. The studies conducted in this thesis for the validation of the CFD methodology are as follows. The analysis of grid sensitivity and turbulence model sensitivity was performed, and the flow field and friction factor were compared. The analysis based on the turbulent Prandtl number of liquid sodium was performed, and an appropriate turbulent Prandtl number was proposed and used in the analysis. Finally, the CFD analysis was performed based on the model selected through sensitivity analysis, and the temperature values measured at the same thermocouple location as in the experiment were compared and analyzed.

## 2. Test Section Description

*2.1. Introduction of PLANDTL Facility.* The Plant dynamics test loop (PLANDTL) facility was developed in the Reactor Engineering Section of PNC, OEC. The construction of this test facility was completed in September 1987, after which various thermal-hydraulic experiments such as the simulation of the LOPI condition of MONJU (PNC demo fast breeder reactor) FBR were conducted at this facility. At the PLANDTL facility, various researchers conducted sodium flow studies. Among them, the test case referenced in this study is a PNC report, LOF-15057, compiled in 1992 by Hayafune and Kabir [2].

Sodium boiling tests have been performed not only at the PLANDTL facility but also at various facilities such as SIENA and DHB. Among them, in the experimental case of this study, test section 37I of the PLANDTL test section and test section 37J of test section 37J were adopted. This test section has a heated length of 930 mm and is heated under heat flux conditions with a chopped cosine distribution of 1:1.204, the ratio of the average to the maximum flux. The wire-wrapped fuel assembly specification of the PLANDTL facility was manufactured with almost the same specifications as the fuel assembly of the MONJU reactor. Pins with a P/D ratio of 1.21 are arranged in a triangular space, and spiral wire spacers with a lead pitch of 307 mm and a diameter of 1.32 mm are wound around each pin. The pin bundle is installed in a hexagonal duct manufactured from Inconel-600 with a thickness of 10 mm. The hexagonal duct is an Inconel tube with a thickness of 10 mm, and the distance between the peripheral pins and the duct wall is approximately 1.5 mm. Detailed geometric information is shown in Table 1. Heat loss through the duct wall was minimized by installing an insulating material on the outer wall of the hexagonal duct. In order to model the shape in the same way as the test section, the relative positions of the wire spacers in each section were all the same as in the test section.

TABLE 1: Geometric information of 37-pin fuel bundle at the PLANDTL facility [2].

Geometry	Values
Number of pins	37
Pin diameter	6.5 mm
Wire diameter	1.32 mm
Wire lead pitch	307 mm
Pin pitch	7.87 mm
P/D	1.21
H/D	47.23
$D_h$	3.4013 mm
Flow area	921.4 mm <sup>2</sup>
Total length of pins	2988 mm
Length of the heated region	930 mm
Duct thickness	10 mm, Inconel
Wire rotation	Clockwise

Figure 1 shows a schematic diagram of the PLANDTL facility. The PLANDTL 37-pin wire-wrapped bundle consists of primary and secondary heat exchangers driven by an electromagnetic pump and thermally connected via an intermediate heat exchanger. In the primary loop, sodium flows into a tank simulating the inlet plenum of the reactor vessel before entering the test section consisting of two separate 37-pin bundles (37I, 37J). Sodium passing through the 37-pin bundle flows to the upper plenum and then to the IHX. The heat generated by the electric heater in the test section is transferred to the secondary loop through the IHX and released to the atmosphere through the air cooler in the secondary loop [6]. The surface temperatures around the sodium and wire spacer in the fuel bundle of the test section were measured with 166 thermocouples on 51 height axes.

**2.2. Features of PLANDTL Facility.** In this experiment, which was conducted to simulate a hypothetical accident, the simultaneous failure of the primary pump and the reactor shutdown system is assumed. The PLANDTL facility, which could be used to carry out these tests, has the following features: [2]

- (1) The facility has a primary and secondary loop as well as a section containing a reactor core simulator, which made it possible to conduct thermal transient experiments including the examination of typical plant system dynamics
- (2) The core simulator consists of two parallel channels, which allow the effect of the thermal transient hydraulic interaction between the core and plenum to be analyzed during transient experiments owing to the difference between the conditions of the two channels
- (3) The facility allows the flow rate and power of the pin bundle to be controlled using the computer system, thus enabling transient sodium boiling experiments to be conducted using a wide combination of parameters

- (4) Controlling the plant with the computer system enables plant dynamics experiments to be conducted, taking into account the negative and positive reactivity feedback effects of the reactor system by modulating the pin power calculated by modeling the reactivity feedback

**2.3. Overview of Experiment No. 15057.** At the PLANDTL facility, experiment no. 15057 was conducted to investigate the behavior of sodium boiling during the test section of the unprotected loss-of-flow event [2]. There were 37 heater pins inside the test section, but 3 pins were damaged during the previous test and remained unheated, leaving only 34 heated pins in total [2]. The unheated pins are 403, 410, and 411 and are shown as gray pins in Figure 2.

In the initial steady state, the heater pins are heated with a total power of 100 kW, and liquid sodium at 398.8°C flows through the test section at 0.3407 m/s. Experiment no. 15057 was performed with a coast-down method in which the pump was turned off after reaching the initial steady state and the flow rate is reduced according to a predetermined flow rate reduction characteristic. The flow rate was reported to decrease from a maximum of 0.3407 m/s to 0.001 m/s within 6.5 s after the onset of the transient.

As the flow rate decreased with the coast down, the temperature inside the test section increased, and after some time, the sodium began to boil. This experiment was conducted for 180 seconds after the onset of the transient, during which time the total power of the test section was held constant at 100 kW.

**2.4. Analysis of Experimental Result.** The test section is installed on a total of 51 axes at different positions in the axial direction, as shown in Figure 3, and totally 166 thermocouples are installed separately in each section. As shown in Figure 3, the maximum number of thermocouples is installed in the BJ section and the BS section, and the temperature distribution in the radial direction can be found using these thermocouples. Among them, the section in which the most thermocouples are installed is the BS section, which is at the top of the heated section, and although it is stated that 33 thermocouples are installed, data for 31 thermocouples were actually provided. In the BS section, the type of thermocouple installed on each wire is different. The summary of each thermocouple type will be analyzed in the following chapter. The numbers of the pins for which thermocouple temperature information is not provided are shown in red in Figure 2. Figure 4 shows the positions of the BS, BN, BJ, and BA sections: the BA section is the heating start position, the BN and BJ sections are located in the middle of the heated section, and the BS section is at the top of the heated section. In order to ensure that the positions of the thermocouple and wire spacer are the same as in the experiment, CFD modeling was used with the same relative positions of the duct and wire. Figure 5 shows the radial temperature at the top of the heated section, as described in the experimental report. These temperature mapping curves are presented in 5-second intervals from 0 to 40 seconds.

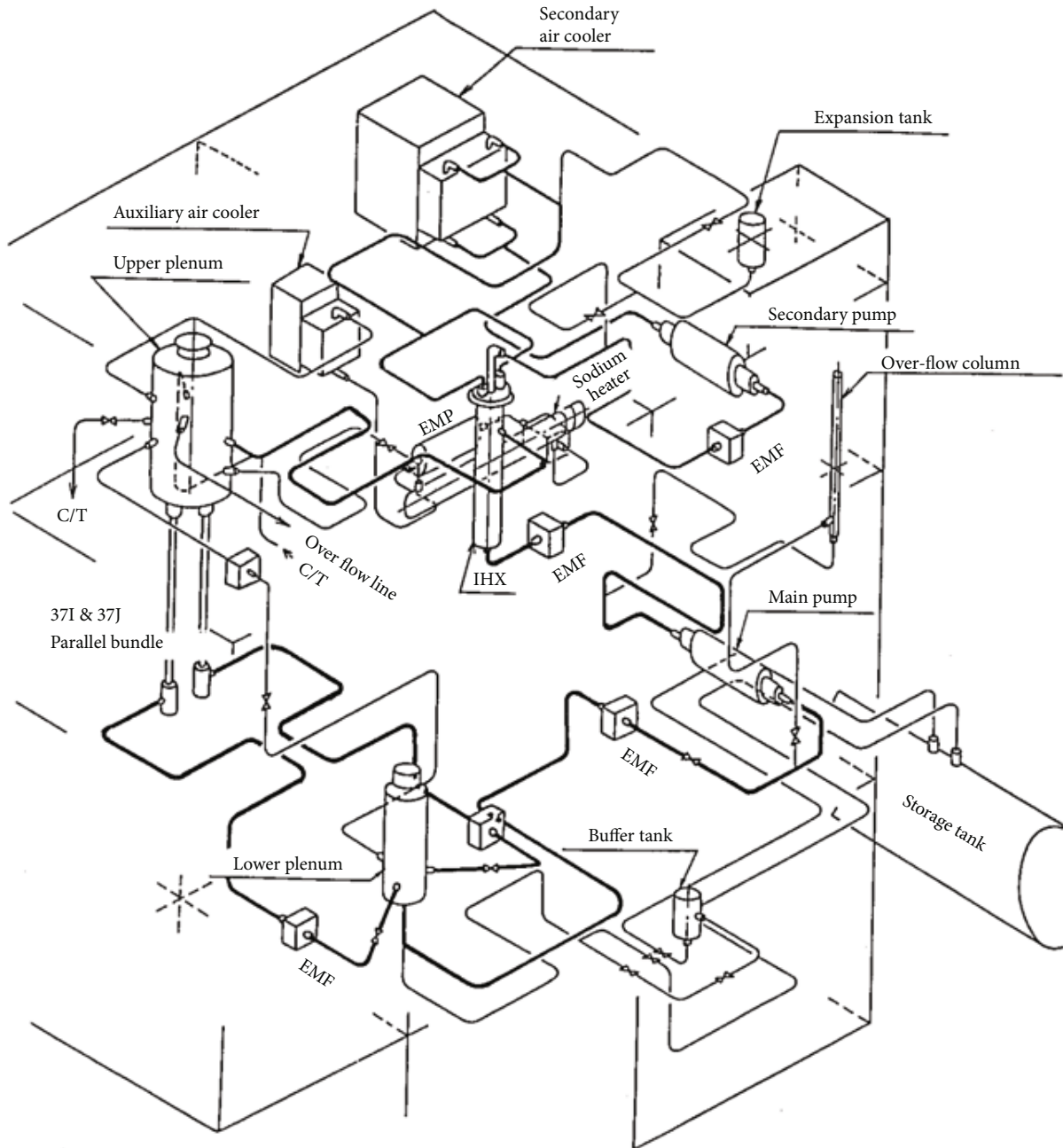


FIGURE 1: Schematic view of PLANDTL facility [2].

### 3. Numerical Method

Table 2 shows the computational boundary conditions of the CFD analysis. The surface of the rods and wire spacers is defined with a no-slip condition with a smooth roughness. The duct wall is also applied under a no-slip condition with a smooth roughness. In the steady state, sodium with an inlet temperature of 398.8°C flows through the test section at a velocity of 0.3407 m/s, and power of 100 kW is constantly applied. A turbulent Prandtl number ( $Pr_t$ ) of 0.02, derived from previous studies, was used, and the sensitivity analysis for the  $Pr_t$  is presented in detail in the results section [3].

The lengths of the heated and unheated regions are set as shown in Figure 4, and the length of the heated region is subjected to a chopped cosine power distribution. The temperature distribution in the radial direction according to the heated pins was determined by leaving the gray pin in Figure 2 as an unheated pin.

Since the experiment is conducted at a high temperature, the dependence of the properties of sodium on the temperature is also important. Therefore, the property values of sodium were applied as polynomial T, and the property values reported by JAEA in 2005 were used for the property relation formula in Table 3 [7].

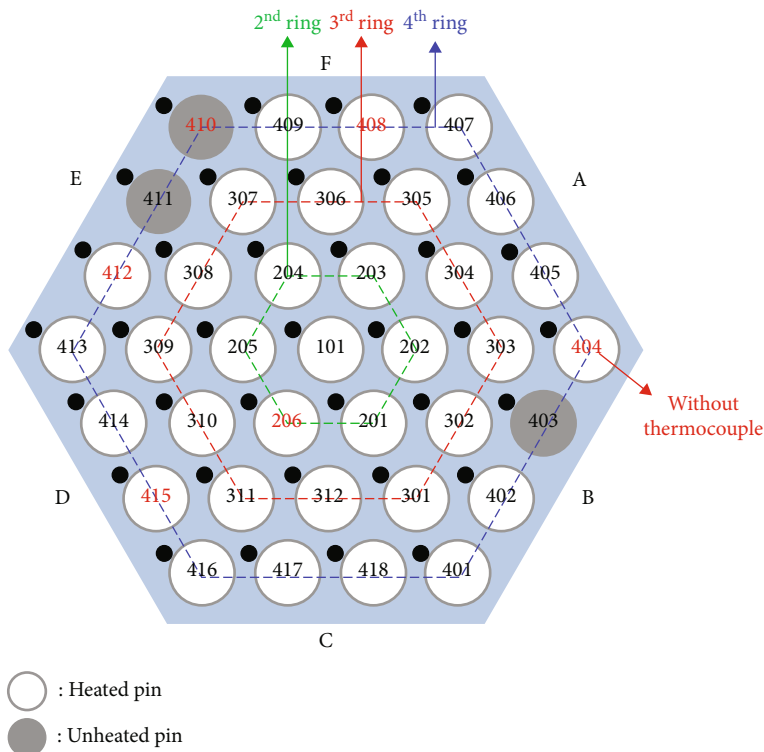


FIGURE 2: Pin numbering and ring numbering along the radial direction (pins with a gray background are unheated, and those numbered in red are not equipped with a thermocouple.)

In the experiments conducted at the PLANDTL facility, thermocouples were used to measure the temperature of the wire, so accurate simulation of the helical wire shape is important. Accurate modeling of the flow phenomenon of the precisely modeled wire-wrapped fuel bundle is critical to simulating the heat transfer phenomenon of the SFR fuel assembly. Most CFD studies or experiments are limited to hydraulic behavior, and heat transfer is typically not included, despite the importance of heat transfer properties. However, the wire-wrapped fuel assembly has numerous contact lines and points between pins and wires, making the geometry complex and the computational mesh difficult to generate. This was accomplished using an innovative grid generation method using Fortran-based in-house code [3, 4, 8]. This grid generation methodology does not use the mesh generation utility of STAR-CCM+. Instead, a mesh generated based on a Fortran code is imported into STAR-CCM+ for use. Because the actual wire shape is simulated without distorting the shape, a more accurate prediction of the contact area between the wire and the rod becomes possible. In the previous study, an innovative grid-based RANS methodology was applied to the CFX, and the pressure drop and heat transfer were well predicted [4, 9]. The grid that forms around the rod and wire is referred to as the inner fluid domain. The grid system of the region surrounding the repeated inner fluid is referred to as the outer fluid domain. The computational grid shown in Figure 6 is an innovative grid system composed of 19 million fluid regions and 13 million solid regions, and each interface is composed of a conformal mesh. The power of 100 kW is supplied to the inner

wall of the rod as heat flux. Accurate modeling of the conjugate heat transfer is possible through a conformal fluid-solid mesh interface. This innovative mesh system enables conjugate heat transfer analysis of the wire-wrapped fuel bundle with good convergence, even with a small number of grids. In the following session, the grid sensitivity and turbulence model sensitivity of the PLANDTL 37-pin wire-wrapped fuel bundle were analyzed for this grid system.

**3.1. Axial Grid Size Sensitivity Analysis.** The sensitivity of the CFD analysis results according to the grid scale was determined by performing the sensitivity analysis by adjusting the minimum grid size in the axial direction. Coarse axial grids increase the discretization errors. The grid system is shown in Figure 7, and the sensitivity of three grid systems was analyzed. A grid sensitivity analysis was performed under this flow condition because the friction factor matches the UCTD correlation most closely at a Reynolds number of 32,850. Information on each of these grids is given in Table 4. The minimum radial grid spacing of grids A, B, and C is  $1.30 \times 10^{-6}$  mm. The axial grid of Grid A has the largest minimum size and the smallest number of total grids. Compared to other studies with a trimmed shape at the interface between the pin surface and wire surface, this RANS-based flow simulation was carried out without any trimmed shapes. The SST turbulence model was selected to perform the mesh sensitivity analysis. The sensitivity analysis of the turbulence model is described in the next section.

Figure 8 compares the normalized temperature, normalized velocity, pressure, and turbulent kinetic energy (TKE)

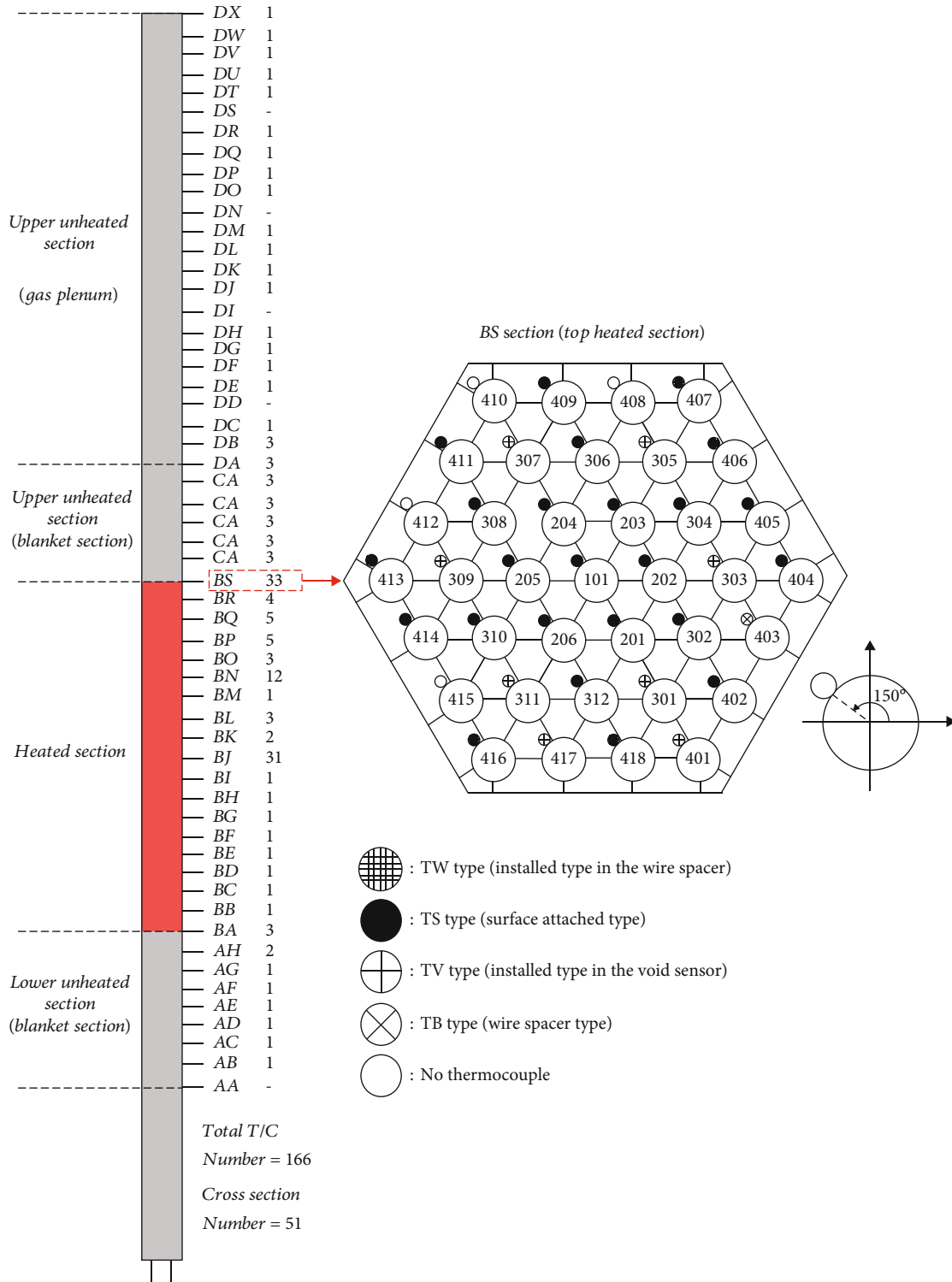


FIGURE 3: Location of thermocouple in the bundle.

components from point A to point B of each grid. Point A is a point at the inlet, and point B is a point at the outlet. As shown in Figure 8, the CFD simulation using the SST turbulence model had no errors due to different axial grid spacing.

Figure 9 compares the friction factors. Many researchers have conducted experiments to derive the friction factor cor-

relation of wire-wrapped rod bundles. The pressure drop on the fully developed flow is calculated as follows:

$$f = \Delta p \frac{D_h}{L} \frac{2}{\rho v^2} \tag{1}$$

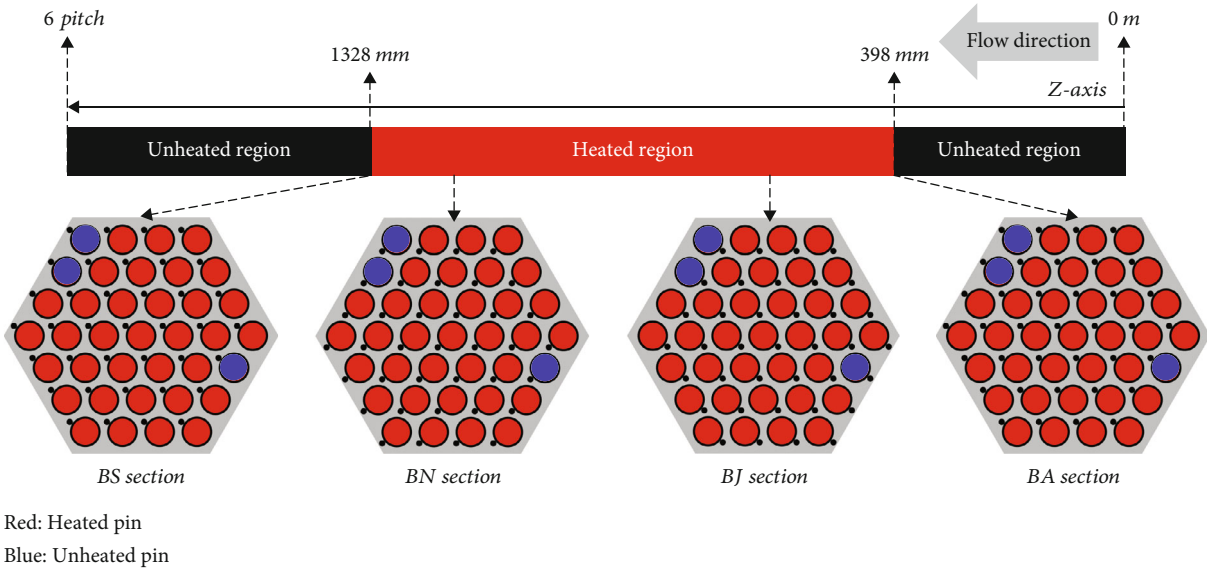


FIGURE 4: Test section for numerical simulation.

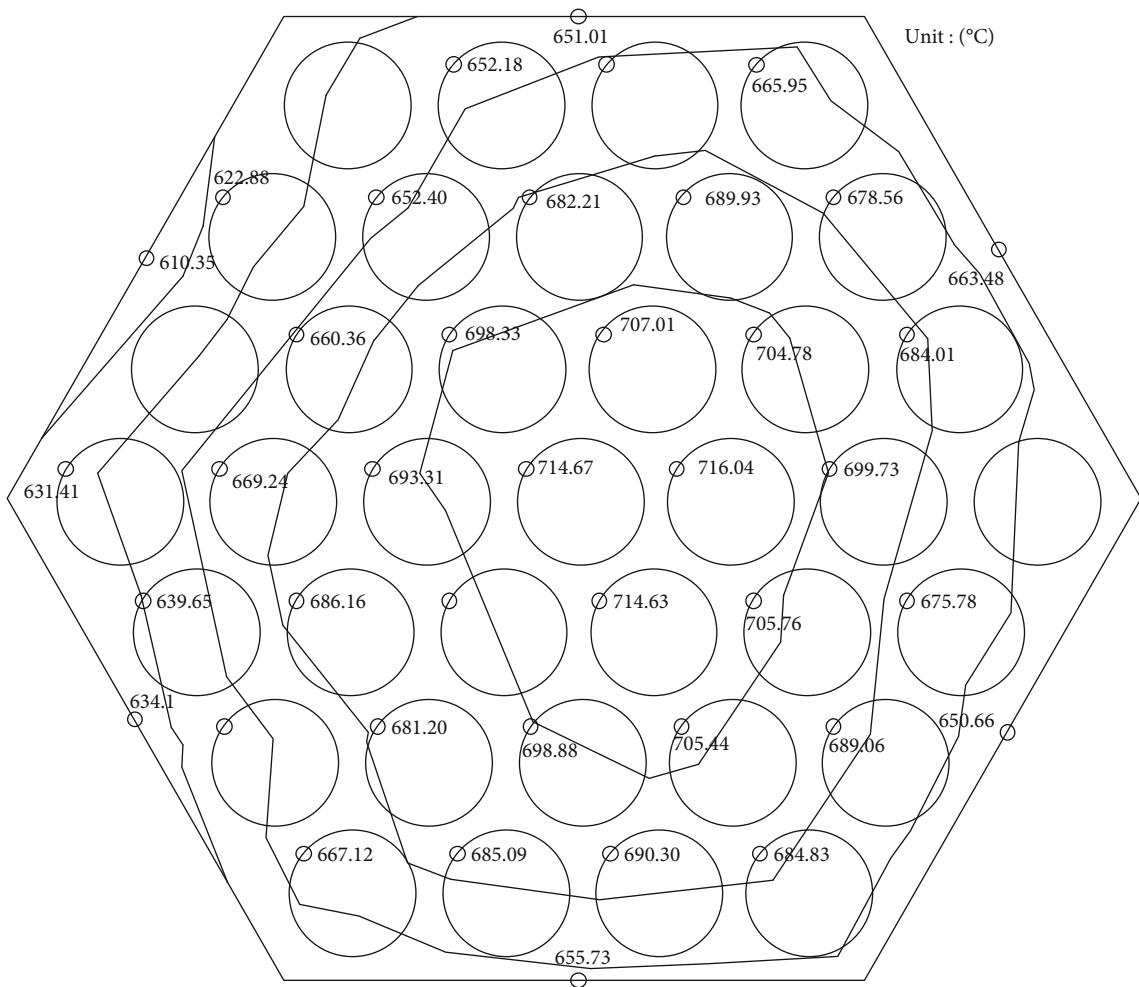


FIGURE 5: Sodium radial temperature mapping curve at the top of the heated section [2].

TABLE 2: Boundary condition of CFD analysis.

Parameters	Values
Inlet velocity	0.3407 m/s
Reynolds number	3,481
Inlet temperature	398.8°C
Total power	100 kW
Turbulent Prandtl number	0.02
Rod, wire	No slip
Duct wall	No slip, adiabatic
Turbulence model	SST model
Coolant	Sodium
Properties of sodium	Polynomial T [7]

Rehme [10], Engel [11], Cheng and Todreas [12], and upgraded Cheng and Todreas [13] have compared the correlations of the friction factor of a fuel assembly in various Reynolds number ranges in detail and evaluated the applicable ranges. Equations (2)–(7) show the correlation expressions. It is important to determine the appropriate correlation equation to be used for the SFR fuel rods and the applicable ranges. The validity range of the friction factor correlation is summarized in Table 5. In this analysis, temperature-dependent properties are used, resulting in varying density values according to temperature. When calculating the friction factor, the density is based on the inlet temperature.

The Rehme correlation [10]

$$f = \left( \left( \frac{64}{\text{Re}} \right) F^{0.5} + \left( \frac{0.0816}{\text{Re}^{0.133}} \right) F^{0.9335} \right) \frac{(\text{Nr})\pi(D + D_w)}{St}, \quad (2)$$

where

$$F = \left( \frac{P}{D} \right)^{0.5} + \left( \frac{7.6(P/D)^2 (D + D_w)}{H} \right)^{2.16}. \quad (3)$$

The Engel correlation [11]

$$\begin{aligned} \text{Laminar flow : } f &= \frac{110}{\text{Re}} \text{ for } \text{Re} \leq 400, \\ \text{Turbulent flow : } f &= \frac{0.55}{\text{Re}^{0.25}} \text{ for } \text{Re} \geq 5000. \end{aligned} \quad (4)$$

The simplified Cheng and Todreas correlation [12]

$$\begin{aligned} \text{Laminar flow : } f &= \frac{C_{fL}}{\text{Re}} \text{ for } \text{Re} \leq \text{Re}_L, \\ \text{Turbulent flow : } f &= \frac{C_{fT}}{\text{Re}^{0.18}} \text{ for } \text{Re}_T \leq \text{Re}, \end{aligned} \quad (5)$$

where

$$\begin{aligned} \text{Re}_L &= 300 \left( 10^{1.7(P/D-1.0)} \right) \\ \text{Re}_T &= 10,000 \left( 10^{0.7(P/D-1.0)} \right) \\ C_{fL} &= \left( -974.6 + 1612.0 \left( \frac{P}{D} \right) - 598.5 \left( \frac{P}{D} \right)^2 \right) \\ &\quad \cdot \left( \frac{H}{D} \right)^{0.06-0.085(P/D)}, \\ C_{fT} &= \left( 0.8063 - 0.9022 \left( \log \frac{H}{D} \right) \right) \\ &\quad + 0.3526 \left( \log \left( \frac{H}{D} \right)^2 \right) * \left( \frac{P}{D} \right)^{9.7} \left( \frac{H}{D} \right)^{1.78-2.0(P/D)}. \end{aligned} \quad (6)$$

The detailed upgraded Cheng and Todreas correlation [13]

$$\begin{aligned} \text{Laminar flow : } f &= \frac{C_{fL}}{\text{Re}} \text{ for } \text{Re} \leq \text{Re}_L, \\ \text{Turbulent flow : } f &= \frac{C_{fT}}{\text{Re}^{0.18}} \text{ for } \text{Re}_T \leq \text{Re}, \end{aligned} \quad (7)$$

where

$$\begin{aligned} C_{fL} &= De_b \left( \sum_{i=1}^3 \left( \frac{N_i A_i}{A_b} \right) \left( \frac{De_i}{De_b} \right) \left( \frac{De_i}{C_{fiL}} \right) \right)^{-1}, \\ C_{fT} &= De_b \left( \sum_{i=1}^3 \left( \frac{N_i A_i}{A_b} \right) \left( \frac{De_i}{De_b} \right)^{0.0989} \left( \frac{De_i}{C_{fiT}} \right)^{0.54945} \right)^{-1.82}, \end{aligned} \quad (8)$$

where  $i = b, 1, 2,$  or  $3$  for the bundle average, interior, edge, and corner subchannels.

Figure 9(a) compares the results of the 37-pin wire-wrapped fuel bundle CFD analysis with the friction factor correlations. The CFD result was most closely fitted by the UCTD correlation. The UCTD correlation is reported to provide the most accurate analysis of the pressure drop of wire-wrapped fuel rod bundles. Figure 9(b) shows the CFD results with the 15% error range of the UCTD correlation. Rolfo et al. also reported that the friction factor calculated by the CFD analysis is in good agreement with the model of Cheng and Todreas model for various cases, which supports this result [14]. This result corresponds with that of previous studies in that a high friction factor tends to be predicted for the low Reynolds range, and the error with the UCTD correlation tends to decrease as the Reynolds number increases. The error in the friction factor for the lowest Reynolds number is 5.6%. As shown in Table 4, the error between grids A, B, and C in the range of  $\text{Re} = 32,850$  is negligible, and the error with UCTD is also less than 1%.

TABLE 3: Properties of sodium (the temperature in the equation is in Celsius units.) [7].

Properties	Function	Unit
Density	$\rho = 1000 \times (0.9501 - 2.2976E - 4 \times T - 1.46E - 8 \times T^2 + 5.638E - 12 \times T^3)$	kg/m <sup>3</sup>
Dynamic viscosity	$\mu = 0.001 \times (0.1235 \pm 0.0018)\rho^{1/3} \times \exp [(697 \pm 9) \rho/T]: T \leq 500^\circ\text{C}$ $\mu = 0.001 \times (0.0851 \pm 0.0013)\rho^{1/3} \times \exp [(1040 \pm 19) \rho/T]: T \geq 500^\circ\text{C}$ (The unit of $\rho$ in dynamic viscosity equation is g/cm <sup>3</sup> )	Pa-s
Thermal conductivity	$\lambda = 100 \times (0.907 - 4.85E - 4 \times T)$	W/m°C
Specific heat	$C_p = 4184 \times (0.34324 - 1.3868E - 4 \times T + 1.1044E - 7 \times T^2)$	J/kg°C

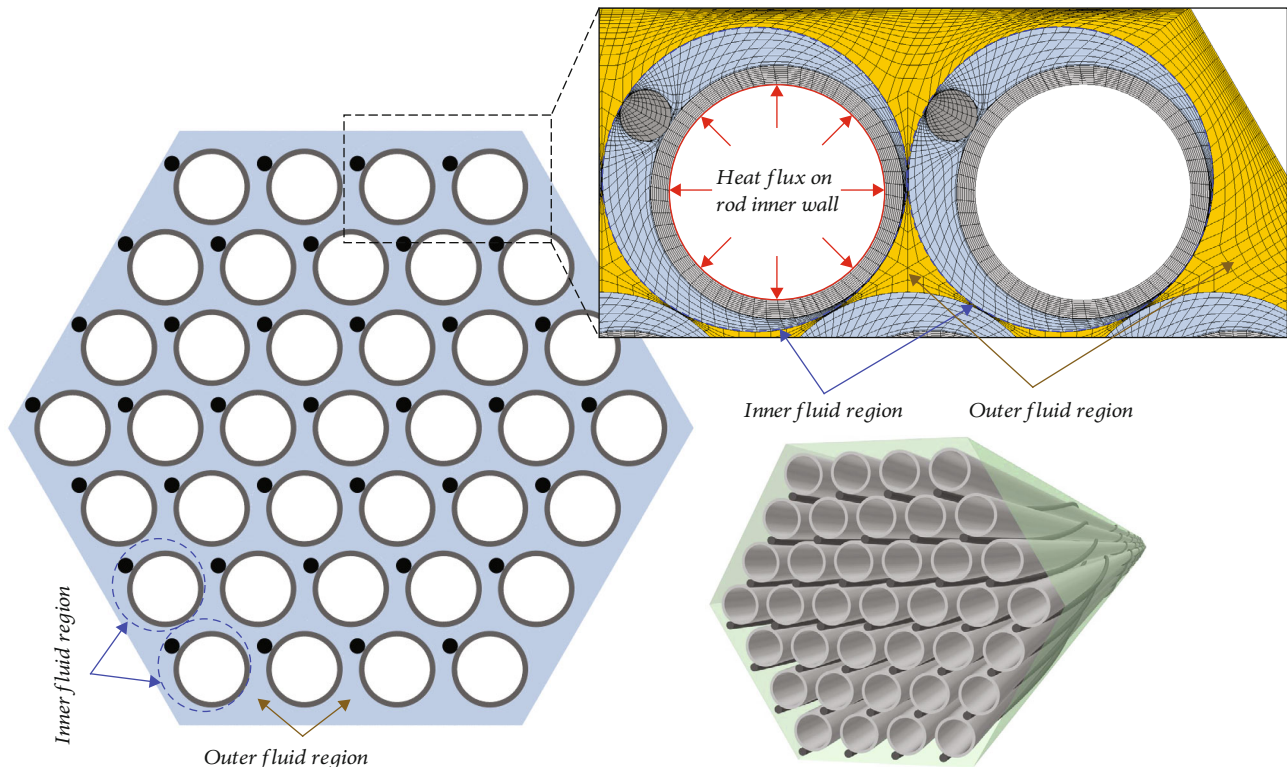


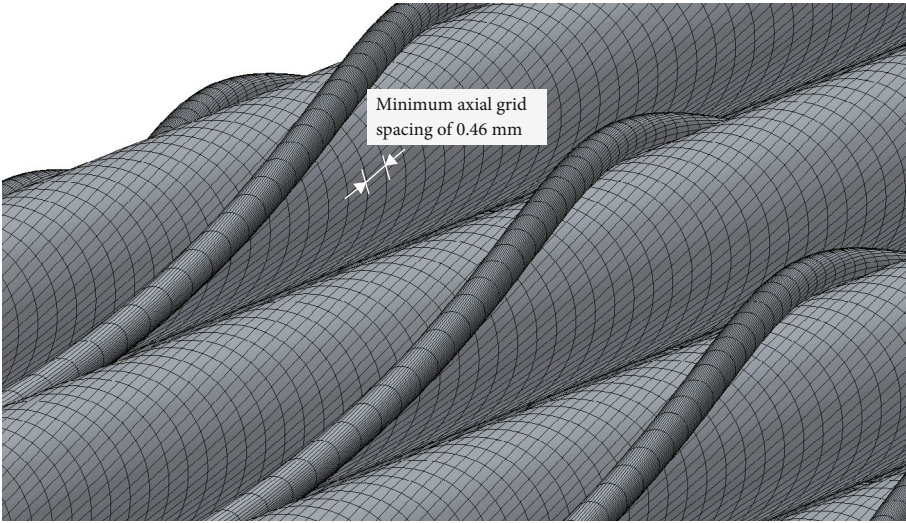
FIGURE 6: Computational grid system of the PLANDTL 37-PIN wire-wrapped fuel bundle.

In the grid used for the axial grid sensitivity analysis, there was no error existed between grids A, B and C, respectively. Therefore, based on the steady-state analysis, it can be concluded that the analysis results do not differ significantly even when the minimum axial grid size is set to a maximum of 0.46 mm.

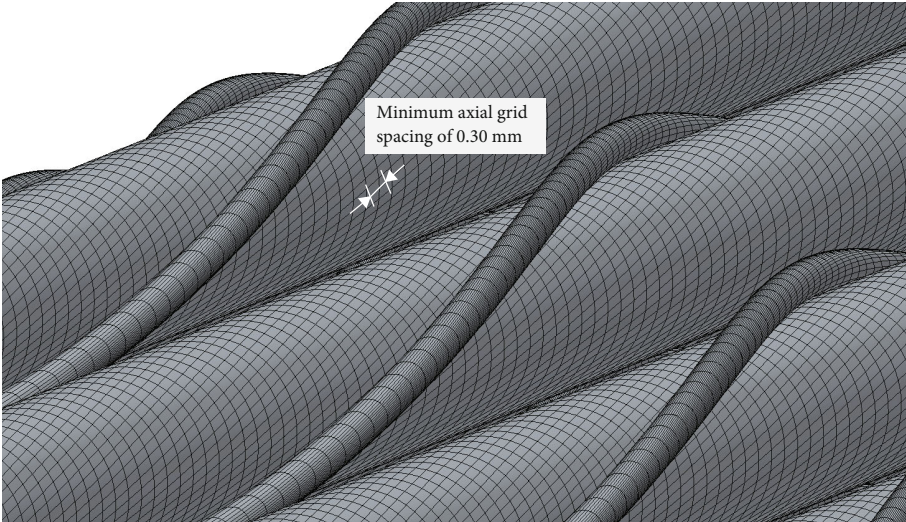
**3.2. Radial Grid Size Sensitivity Analysis.** In the study described in the previous section, it was confirmed that the flow field and temperature fields are independent of the axial grid size. In addition, according to the previous JAEA study, which included a CFD investigation on a 127-pin JAEA, the flow and temperature fields were found to be more sensitive to changes in the radial grid size than the axial grid size. Since the  $y^+$  value based on the wall-normal grid spacing directly affects the calculation of the value of the  $w$ -specific dissipation rate in the  $k - \omega$  turbulence model, different grids with various  $y^+$  values were compared. In this session, the sensitivity of the

size of the radial grid was analyzed with a different number of grids normal to the wall to investigate the change in the radial grid size. The grid system and the three grid sizes used for the sensitivity analysis are shown in Figure 10. Information about each grid is given in Table 6. Grids D, E, and F were configured by changing the grid size of the inner fluid wall.

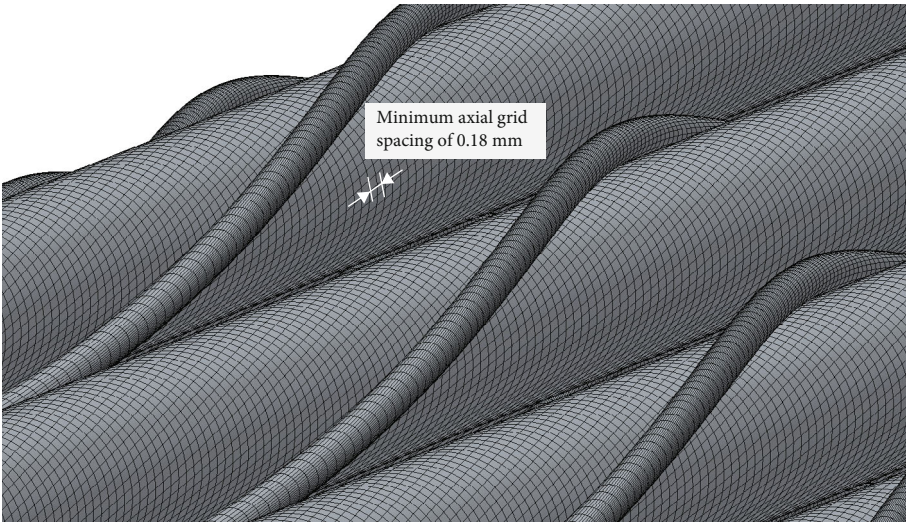
The average  $y^+$  values of grids D, E, and F at  $Re = 32,850$  are 1.88, 0.94, and 0.61, respectively. The minimum distance from the wall to the inner fluid is  $1.25 \times 10^{-6}$  mm,  $4.16 \times 10^{-7}$  mm, and  $2.50 \times 10^{-7}$  mm, respectively. At  $Re = 32,850$ , the errors of the friction factor using the SST turbulence model for different wall grid spacings are 4.26%, 0.80%, and 0.17%, respectively. The method for analyzing the sensitivity of the radial grid size is similar to that reported in Bovati et al. [15], and in this study, the axial velocity and TKE were analysed according to the grid. Figure 11 compares the axial velocity field and TKE between point A and point B. These two points are located between pins 101



(a) Grid A



(b) Grid B

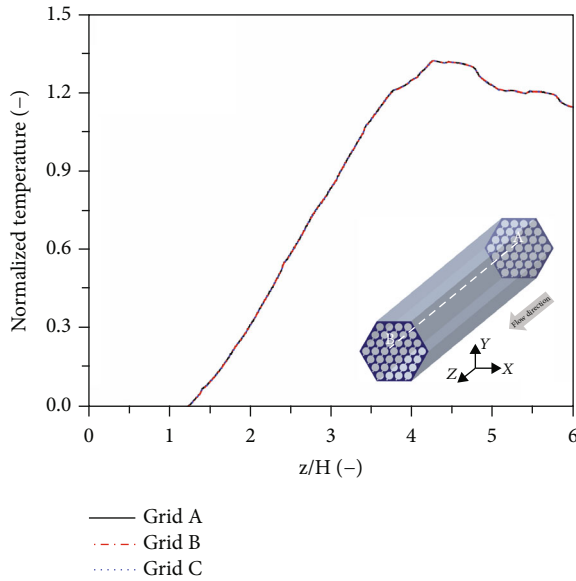


(c) Grid C

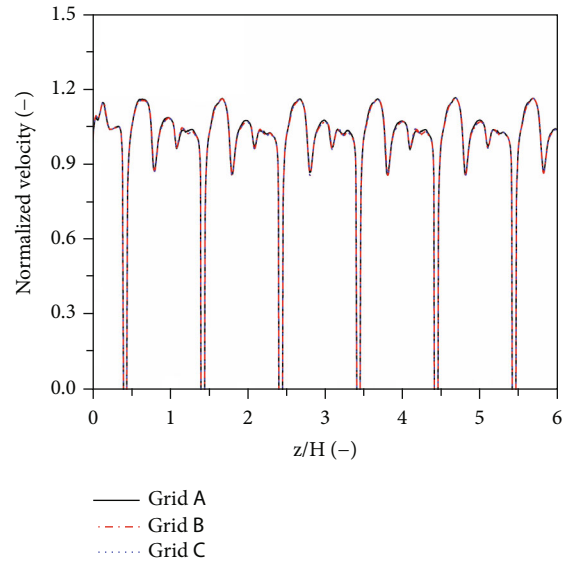
FIGURE 7: Mesh distribution on different axial grid spacings.

TABLE 4: Axial grid sensitivity analysis and friction factor result at  $Re = 32,850$ .

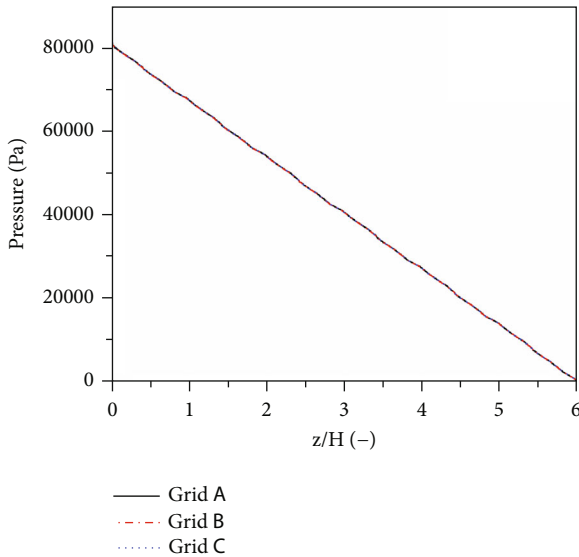
Grid name	Number of cells (fluid region)	Minimum axial grid spacing	Friction factor (CFD)	$\frac{f_{CFD} - f_{UCTD}}{f_{UCTD}}$
Grid A	19.2 M	0.46 mm	0.0229026	0.80%
Grid B	28.6 M	0.30 mm	0.0229037	0.79%
Grid C	48.0 M	0.18 mm	0.0229488	0.60%



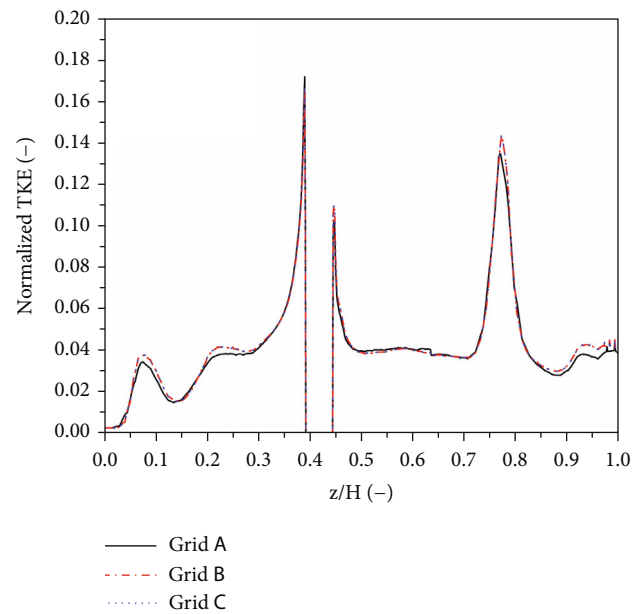
(a) Normalized temperature comparison from point A to point B



(b) Normalized axial velocity comparison from point A to point B



(c) Pressure comparison from point A to point B

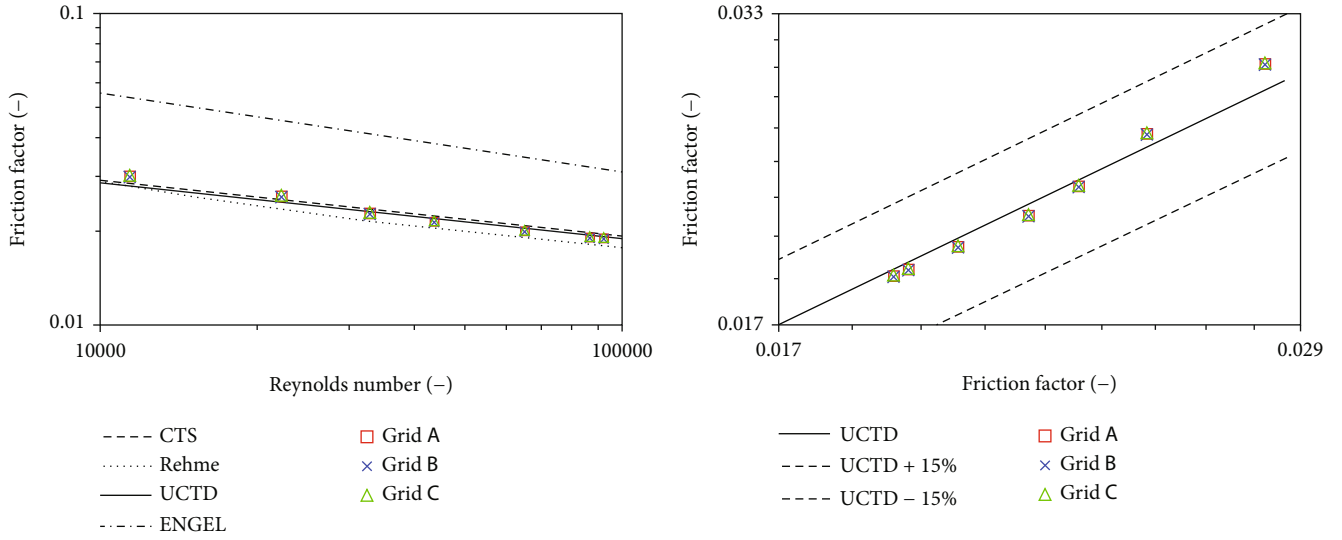


(d) Turbulent kinetic energy comparison from point A to 1 lead pitch

FIGURE 8: Comparison of axial components of grids A, B, and C.

and 203, respectively. In Figure 11(a), which compares the normalized velocity, the results for the three grid systems are the same. In Figure 11(b), which compares the TKE results, there is a difference of about 7.8% between grid D and grid F exists at the maximum peak value, but the other graphs appear to show the same trends. It was confirmed

that there is a small difference in the friction factor,  $y^+$  value, and the flow field in all grids D, E, and F, and appropriate convergence results were obtained for each grid. Therefore, the grid system selected for analysis in this study, with a minimum axial grid size of 0.30 mm and an average  $y^+$  value of 0.94, was confirmed to be appropriate.



(a) Pressure drop comparison of correlations and CFD results with grids A, B, and C for a range of Reynolds numbers

(b) Comparison within an error of  $\pm 15\%$  of UCTD correlation

FIGURE 9: Friction factor correlations in the 37-pin wire-wrapped fuel bundle.

TABLE 5: Application range and database for friction factor correlations.

Model	$N_r$	$P/D$	$H/D$	Reynolds number range	Uncertainty
Rehme [10]	7~217	1.1~1.42	8.0~50.0	1000 ~ $3 \times 10^5$	$\pm 8\%$
Engel [11]	19~61	1.067~1.082	7.7~8.3	All regimes ( $50 \sim 10^6$ )	$\pm 15\%$
CTS [12]	19~217	1.025~1.42	8.0~50.0	All regimes ( $50 \sim 10^6$ )	$\pm 15\%$
UCTD [13]	7~271	1.000~1.420	8.5~52.0	All regimes ( $50 \sim 10^6$ )	$\pm 15\%$

**3.3. Turbulence Model Sensitivity Analysis.** Three major numerical techniques can be used to analyze turbulent flow fields: direct numerical simulation (DNS), large eddy simulation (LES), and Reynolds-averaged Navier-Stokes (RANS) simulation. RANS uses time-based, ensemble-averaged Navier-Stokes equations, and models all of the effects from turbulence. Although RANS yields a lower-resolution analysis than DNS or LES, it is widely used in engineering applications due to the practical aspect of not requiring high-resolution computational grids. The turbulence models for the RANS equations are for computing the Reynolds stress tensor from the turbulent fluctuations in the fluid momentum. The computational cost of DNS and LES increases with the cube and square of the Reynolds number. Therefore, taking into consideration the computational resources, a RANS simulation was adopted for the CFD analysis in this study [5].

The STAR-CCM+ software package includes various built-in turbulence models such as  $k-\epsilon$ ,  $k-\omega$ , Reynolds stress turbulence, and Spalart-Allmaras turbulence [16]. It is necessary to analyze the sensitivity of the model. The  $k-\epsilon$  turbulence model accurately predicts the turbulence behavior in the free turbulence region where the pressure gradient is small, but the boundary layer separation prediction in the viscous low layer region is inaccurate. Wilcox's  $k-\omega$  turbulence model accurately predicts delamination due to reverse pressure gradients but is sensitive to inflowing free turbulence. Therefore, Menter proposed the SST model

using only the advantages of the  $k-\epsilon$  and  $k-\omega$  turbulence models. In this study, to understand the sensitivity of STAR-CCM+, the sensitivity to three turbulence models such as  $k-\epsilon$ ,  $k-\omega$ , and SST was investigated.

Turbulence models such as  $k-\epsilon$ ,  $k-\omega$ , and SST have become industry standard models and are commonly used for most types of engineering problems. The SST model solves the above problems for switching to the  $k-\epsilon$  model in the free-stream and the  $k-\omega$  model in the viscous sub-layers. The sensitivity of turbulence models such as the Reynolds stress model (RSM),  $k-\epsilon$ ,  $k-\omega$ , and SST has been investigated 127-pin and 61-pin fuel assemblies. In that study, the friction factors with the SST model are 1.5–4.5% higher than that with the  $k-\epsilon$  model. The friction factor with the SST model is 1.4–1.5% lower than that with the  $k-\omega$  model. Because the SST model switches to the  $k-\epsilon$  model and the  $k-\omega$  model, the value of the friction factor with the SST model is between that with the  $k-\epsilon$  model and that with the  $k-\omega$  model [5].

In this session, realizable  $k-\epsilon$ , standard  $k-\epsilon$ , standard  $k-\omega$ , and SST  $k-\omega$  (Menter) models were used to analyze the changes in the flow and temperature fields for each model. As in the previous session, Figure 12 shows the normalized axial velocity and TKE. In Figure 12(a), the same velocity field was also observed for all  $k-\epsilon$  models as well. The maximum normalized axial velocity differed for the  $k-\omega$  and  $k-\epsilon$  models, with the prediction of the  $k-\epsilon$

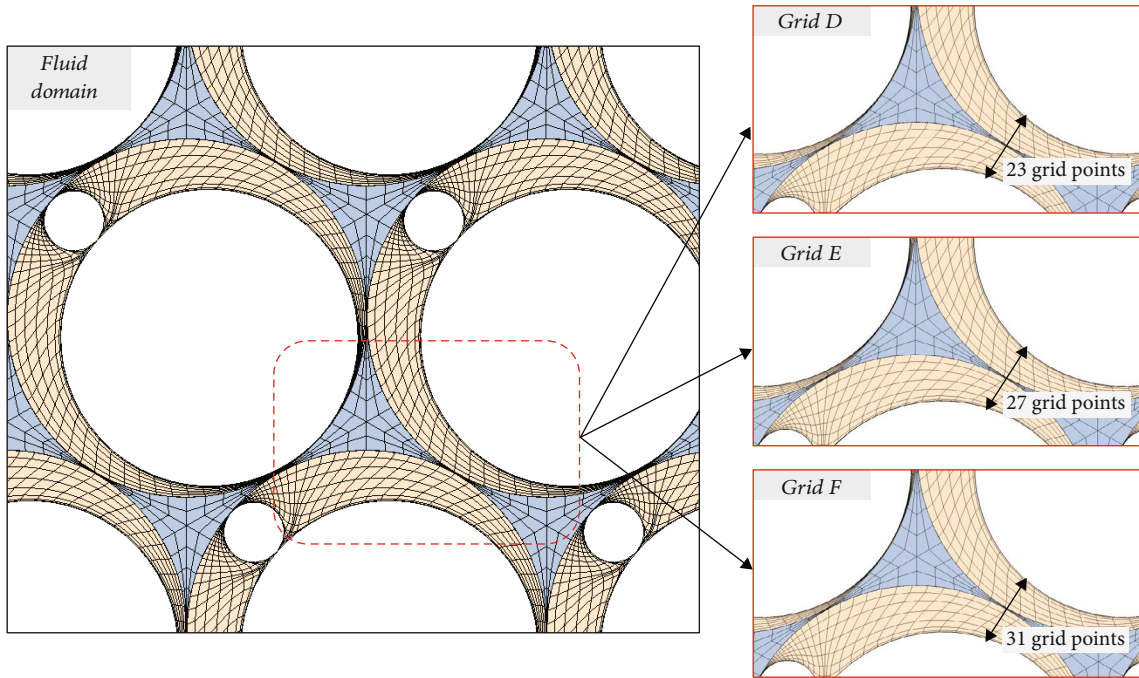


FIGURE 10: Mesh distribution on different radial grid spacings.

TABLE 6: Radial grid sensitivity analysis and friction factor result at  $Re = 32,850$ .

Grid name	Number of cells	Radial grid points	Max $y^+$	Average $y^+$	Min $y^+$	Minimum scale from wall	Friction factor (CFD)	$\frac{f_{CFD} - f_{UCTD}}{f_{UCTD}}$
Grid D	29.5 M	23	22.3	1.88	0.27	$1.25 \times 10^{-6}$	0.0221037	4.26%
Grid E	32.5 M	27	10.5	0.94	0.062	$4.16 \times 10^{-7}$	0.0229026	0.80%
Grid F	35.5 M	31	4.42	0.61	0.023	$2.50 \times 10^{-7}$	0.0230485	0.17%

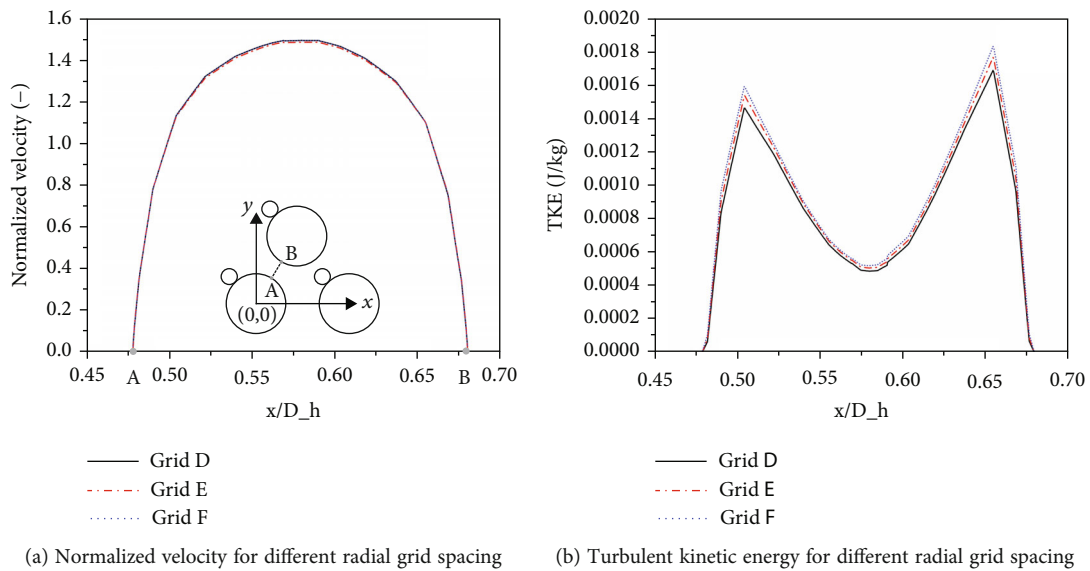


FIGURE 11: Flow field comparison from point A to point B for different radial grid spacing.

model lower than that of the  $k - \omega$  model. Figure 12(b) compares the TKE results, with the maximum TKE predicted by the  $k - \omega$  model tending to be approximately 50% lower than

that of the  $k - \epsilon$  model. The TKE of the  $k - \epsilon$  model is derived to be larger, and this large TKE promotes the mixing effect of the wire spacer, such that the thermal mixing is more effective.

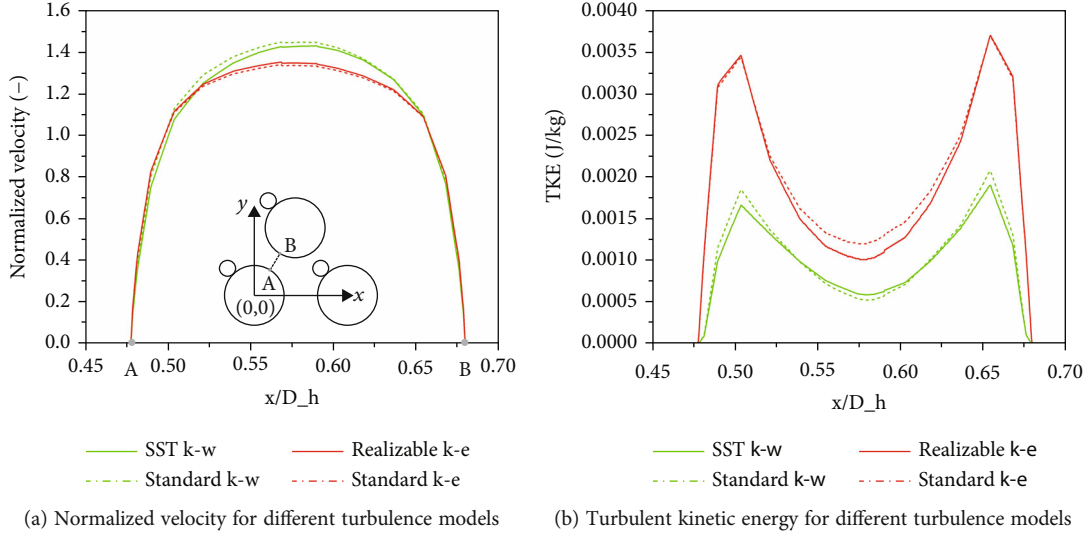


FIGURE 12: Flow field comparison from point A to point B for different turbulence models.

The difference in turbulent kinetic energy between the  $k-\epsilon$  model and the  $k-\omega$  model is due to the difference in production term. The transport equation of the  $k-\epsilon$  model is as follows [16]:

$$\frac{\partial}{\partial t}(\rho k) + \nabla \cdot (\rho k \bar{\mathbf{v}}) = \nabla \cdot \left[ \left( \mu + \frac{\mu_t}{\sigma_k} \right) \nabla k \right] + P_k - \rho(\epsilon - \epsilon_0) + S_k, \quad (9)$$

$$\begin{aligned} \frac{\partial}{\partial t}(\rho \epsilon) + \nabla \cdot (\rho \epsilon \bar{\mathbf{v}}) = \nabla \cdot \left[ \left( \mu + \frac{\mu_t}{\sigma_\epsilon} \right) \nabla \epsilon \right] + \frac{1}{T_e} C_{\epsilon 1} P_\epsilon \\ - C_{\epsilon 2} f_2 \rho \left( \frac{\epsilon}{T_e} - \frac{\epsilon}{T_0} \right) + S_\epsilon. \end{aligned} \quad (10)$$

The transport equation of the  $k-\omega$  model is as follows:

$$\frac{\partial}{\partial t}(\rho k) + \nabla \cdot (\rho k \bar{\mathbf{v}}) = \nabla \cdot [(\mu + \sigma_k \mu_t) \nabla k] + P_k - \rho \beta^* f_\beta (\omega k - \omega_0 k_0) + S_k \quad (11)$$

$$\frac{\partial}{\partial t}(\rho \omega) + \nabla \cdot (\rho \omega \bar{\mathbf{v}}) = \nabla \cdot [(\mu + \sigma_\omega \mu_t) \nabla \omega] + P_\omega - \rho \beta f_\beta (\omega^2 - \omega_0^2) + S_\omega \quad (12)$$

The  $P_k$  is the production of turbulent kinetic energy from the shear strain rate. The  $P_\epsilon$  is the production of turbulent dissipation rate  $\epsilon$  in order to determine the turbulent eddy viscosity.

The formulation of the production terms  $P_k$  and  $P_\epsilon$  depends on the standard  $k-\epsilon$  model variant:

$$\begin{aligned} P_k &= G_k + G_{nl} + G_b - \gamma_M, \\ P_\epsilon &= G_k + G_{nl} + C_{\epsilon 3} G_b, \end{aligned} \quad (13)$$

The formulation of the production terms  $P_k$  and  $P_\epsilon$

depends on the realizable  $k-\epsilon$  model variant:

$$\begin{aligned} P_k &= f_c G_k + G_b - \gamma_M, \\ P_\epsilon &= f_c S_k + C_{\epsilon 3} G_b. \end{aligned} \quad (14)$$

$G_k$  is turbulent production,  $G_{nl}$  is nonlinear production,  $G_b$  is buoyancy production, and  $\gamma_M$  is compressibility modification, where

$$\begin{aligned} G_k &= \mu_t S^2 - \frac{2}{3} \rho k \nabla \cdot \bar{\mathbf{v}} - \frac{2}{3} \mu_t (\nabla \cdot \bar{\mathbf{v}})^2, \\ G_b &= \beta \frac{\mu_t}{Pr_t} (\nabla \bar{T} \cdot \mathbf{g}), \\ G_{nl} &= \nabla \cdot \bar{\mathbf{v}}, \\ \gamma_M &= \frac{\rho C_M k \epsilon}{c^2}. \end{aligned} \quad (15)$$

The formulation of the production terms  $P_k$  and  $P_\epsilon$  depends on the standard  $k-\omega$  model variant:

$$\begin{aligned} P_k &= G_k + G_b, \\ P_\omega &= G_\omega. \end{aligned} \quad (16)$$

The formulation of the production terms  $P_k$  and  $P_\epsilon$  depends on the SST  $k-\omega$  model variant:

$$\begin{aligned} P_k &= G_k + G_{nl} + G_b, \\ P_\omega &= G_\omega + D_\omega. \end{aligned} \quad (17)$$

$G_\omega$  is specific dissipation production, and  $D_\omega$  is cross-

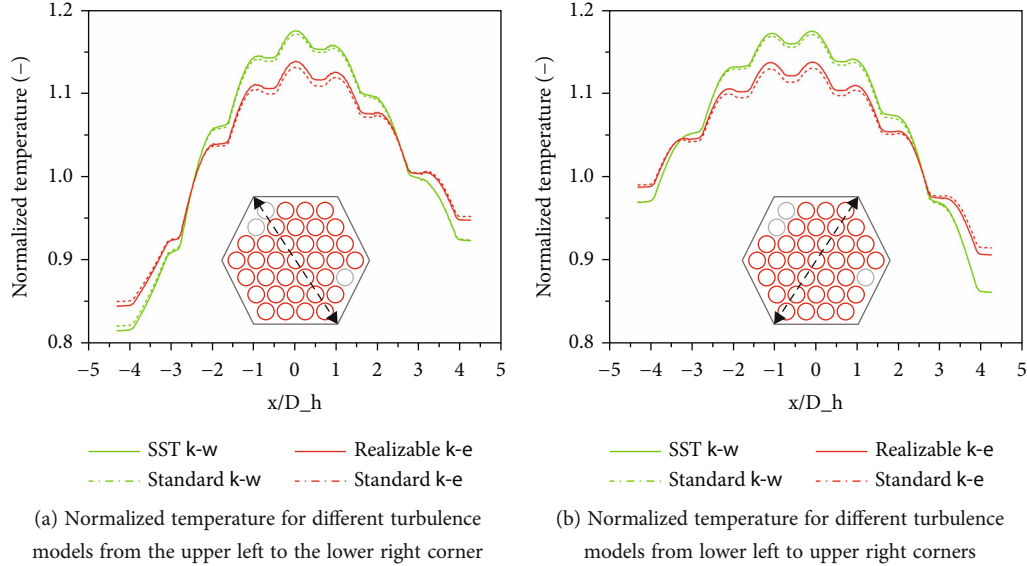


FIGURE 13: Temperature field comparison from point A to point B for different turbulence models.

diffusion term, where

$$\begin{aligned}
 G_k &= \mu_t f_c S^2 - \frac{2}{3} \rho k \nabla \cdot \bar{\mathbf{v}} - \frac{2}{3} \mu_t (\nabla \cdot \bar{\mathbf{v}})^2, \\
 G_b &= \beta \frac{\mu_t}{Pr_t} (\nabla \bar{T} \cdot \mathbf{g}), \\
 G_{nl} &= \nabla \cdot \bar{\mathbf{v}}, \\
 G_\omega &= \begin{cases} \text{Standard } k-\omega : \rho \alpha \left[ \left( \alpha^* S^2 - \frac{2}{3} (\nabla \cdot \bar{\mathbf{v}})^2 \right) - \frac{2}{3} \omega \nabla \cdot \bar{\mathbf{v}} \right], \\ \text{SST } k-\omega : \rho \gamma \left[ \left( S^2 - \frac{2}{3} (\nabla \cdot \bar{\mathbf{v}})^2 \right) - \frac{2}{3} \omega \nabla \cdot \bar{\mathbf{v}} \right], \end{cases} \\
 D_\omega &= 2\rho(1-F_1)\sigma_{\omega_2} \frac{1}{\omega} \nabla k \cdot \nabla \omega.
 \end{aligned} \tag{18}$$

The production term of the  $k-\varepsilon$  model predicted a larger TKE than the  $k-\omega$  model, which means that the  $k-\varepsilon$  turbulence model predicted the mixing of the fluid by the wire spacer more strongly, resulting in more energy loss. This can be seen from the shape difference of the velocity profile at points A and B between the walls of no. 1 and no. 3 rods in Figure 12(a). The velocity profile of the  $k-\varepsilon$  model was flattened to equalize the velocity.

As shown in Figure 13, due to this effect, the temperature of the  $k-\omega$  model is higher in the central region, and the temperature of the  $k-\varepsilon$  model is higher as it approaches the edge subchannel. In Figure 13(a), the temperature distribution for  $x/D_h < -2$  is different from that of  $x/D_h > 2$ , which is due to the effect of the unheated pins 410 and 411 in the 4th ring. In addition, in Figure 13(b), for  $x/D_h > 2$ , the temperature is low due to the effect of the unheated pin. A detailed analysis of the effect of these unheated pins is given in the following section. There is a clear difference between the velocity field and the temperature field for each turbu-

lence model, which should be analyzed in detail in a follow-up study.

Figure 14 compares the results of the sensitivity analysis of the different turbulence models. Since the pressure drop was not measured in the experiment, only the friction factor was compared with the correlation. Both  $k-\omega$  turbulence models agree well with the UCTD correlation in all regimes, while both  $k-\varepsilon$  models differ from the UCTD correlation. For low Reynolds numbers, both  $k-\varepsilon$  models overestimate compared to the UCTD. The grid used to investigate the axial friction factor of the turbulence model may not be suitable for the standard  $k-\varepsilon$  model because the average  $y^+$  value is less than 1. When considering the functionality of a two-layers all  $y^+$  wall treatment, it is also possible to use a  $k-\varepsilon$  model with the  $y^+ < 1$  mesh. In all flow regimes, the standard  $k-\varepsilon$  model differs from the UCTD. On the other hand, the realizable  $k-\varepsilon$  model includes a new transport equation for the turbulent dissipation rate  $\varepsilon$ . This model is substantially more accurate than the standard  $k-\varepsilon$  model for many applications and can generally be relied upon to provide answers that are at least as accurate. Both  $k-\omega$  models were also able to predict the axial friction factor in the turbulent regime with low error with respect to the UCTD correlation or slightly overestimated them. Based on the results of the sensitivity analysis obtained with the turbulence model, it can be concluded that the SST  $k-\omega$  turbulence model predicted the pressure drop the most accurately. The average  $y^+$  value at  $Re = 91,870$  is 1.90, and the average  $y^+$  values for different Reynolds numbers, where pressure drop is compared, are maintained below 2 in all cases. In addition, most CFD studies of wire-wrapped fuel bundles were performed using the SST turbulence model. Jeong et al.'s results show that the pressure drop results using the SST turbulence model are in best agreement with the correlation equation in previous studies using CFX [4, 5, 17]. Bovati et al. reported that the SST  $k-\omega$  simulation results were suitable for predicting the velocity and pressure fields within wire-wrapped rod bundles through

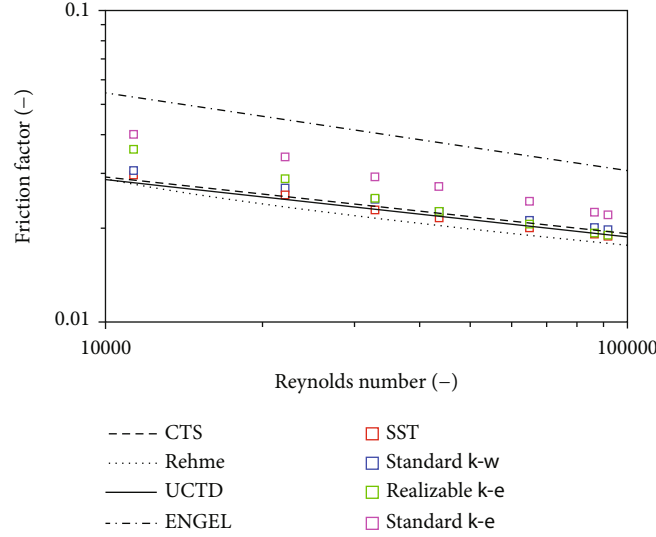


FIGURE 14: Pressure drop comparison of correlations and CFD results with different turbulence models for a range of Reynolds numbers.

comparisons with experimental data and LES [15]. Therefore, the RANS-based SST turbulence model with all  $y^+$  wall treatment was selected for this analysis. The results obtained with this model and those of the grid system derived from the above grid sensitivity analysis were evaluated in comparison with the experimental results.

#### 4. Heat Transfer Result

The CFD analysis was performed using the grid and turbulence model obtained through the grid sensitivity analysis and turbulence model sensitivity analysis described in the previous section. The grid system used for the steady-state analysis adopted a grid with a minimum axial grid spacing of 0.30 mm and average  $y^+$  of 0.94 and is composed of a hexahedral mesh as shown in Figure 6. The fluid, solid, and interface regions have a conformal interface.

In the experiment, a total of four types of sensors and thermocouples were used to measure the temperature. A total of 166 thermocouples are installed in the planes of different axes, and 33 thermocouples are installed in the top of the heated section. The following types of thermocouples are as follows: TW type (installed in the wire spacer), TV type (installed in the void sensor), TS type (attached to the surface), and TB type (spacer wire type). The thermocouple types for each pin number are listed in Table 7. Since the exact temperature measurement location for each type of thermocouple is not shown in the experimental report, the temperature was compared by selecting the measurement location as shown in Figure 15. Of the 37 pins, Figure 15(a) shows only the 7 pins in the center area, and the subchannels adjacent to the wire were selected to compare the temperatures. For example, pin number 101 (subchannel 6) and pin number 201 (subchannel 4) are paired with each other. Figure 15(b) shows the numbering of the subchannels of the 37-pin wire-wrapped fuel bundle. Table 7 compares the resulting normalized temperature, and the error of each component is less than 1%. To com-

pare the temperature of wire and subchannel, the normalized temperature  $\Theta$  is defined in Equation (19).

$$\Theta = \frac{T - T_{in}}{T_{out} - T_{in}}. \quad (19)$$

To reduce the uncertainty introduced by the unknown location of the thermocouple, the results are compared using the average temperature of the subchannel. Therefore, the temperature comparison to the experimental results in this section was made by measuring the temperature of the subchannel. Due to the high thermal conductivity of sodium, there is almost no difference between the temperature at the midpoint of the wire and the average temperature of the subchannel.

As described previously, the temperature of the thermocouple attached to the wire spacer was compared by using the same location for the experimental and CFD results. This section presents the effect of the turbulent Prandtl number ( $Pr_t$ ), the effect of the radial temperature distribution according to the number of heated pins, and a comparison of the experimental and CFD results in the steady state.

*4.1. Comparison of Heat Transfer Correlations with Turbulent Prandtl Number.* Liquid metals, unlike conventional fluids, have a highly complex heat transfer phenomenon due to their low Prandtl number. Accurate prediction of turbulent heat transfer at these low Prandtl numbers is not an easy task using standard turbulence models [18]. The thermal conductivity of liquid metals is several times higher than that of conventional fluids, but the viscosity and Prandtl number of liquid metals are much lower than those of conventional fluids. Therefore, when considering the heat transfer characteristics of liquid metals, heat conduction cannot be neglected in favor of momentum transport and heat transfer. Sometimes thermal diffusion in liquid metals is much larger than viscous diffusion; thus heat conduction plays a dominant role, and the thermal boundary layer is

TABLE 7: Type of thermocouple for each pin and normalized temperature comparison at the wire midpoint and subchannel.

Pin number (TC type)	Numbering	Normalized temperature	Error (%)
Pin 101 (TW)	No. 1 wire	1.147	0.168
	Subchannel 6	1.145	
Pin 201 (TS)	No. 2 wire	1.156	0.084
	Subchannel 4	1.157	
Pin 202 (TS)	No. 3 wire	1.136	0.119
	Subchannel 24	1.137	
Pin 203 (TS)	No. 4 wire	1.099	0.172
	Subchannel 8	1.097	
Pin 204 (TS)	No. 5 wire	1.068	0.508
	Subchannel 24	1.063	
Pin 205 (TS)	No. 6 wire	1.108	0.315
	Subchannel 22	1.104	
Pin 206 (TSS)	No. 7 wire	1.151	0.165
	Subchannel 20	1.149	
Pin 301 (TV)	No. 8 wire	1.100	0.224
	Subchannel 16	1.103	
Pin 302 (TS)	No. 9 wire	1.102	0.411
	Subchannel 14	1.107	
Pin 303 (TV)	No. 10 wire	1.067	0.531
	Subchannel 12	1.073	
Pin 304 (TS)	No. 11 wire	1.077	0.114
	Subchannel 10	1.075	
Pin 305 (TV)	No. 12 wire	1.013	0.630
	Subchannel 28	1.007	
Pin 306 (TS)	No. 13 wire	0.989	0.356
	Subchannel 26	0.986	
Pin 307 (TV)	No. 14 wire	0.923	0.688
	Subchannel 54	0.916	
Pin 308 (TS)	No. 15 wire	0.994	0.384
	Subchannel 52	0.991	
Pin 309 (TV)	No. 16 wire	1.035	0.430
	Subchannel 50	1.030	
Pin 310 (TS)	No. 17 wire	1.095	0.348
	Subchannel 48	1.091	
Pin 311 (TV)	No. 18 wire	1.099	0.269
	Subchannel 46	1.096	
Pin 312 (TS)	No. 19 wire	1.147	0.168
	Subchannel 18	1.145	
Pin 401 (TV)	No. 20 wire	1.156	0.084
	Subchannel 40	1.157	
Pin 402 (TS)	No. 21 wire	1.136	0.119
	Subchannel 38	1.137	
Pin 403 (TB)	No. 22 wire	1.099	0.172
	Subchannel 36	1.097	
Pin 404 (TW)	No. 23 wire	1.068	0.508
	Subchannel 34	1.063	

TABLE 7: Continued.

Pin number (TC type)	Numbering	Normalized temperature	Error (%)
Pin 405 (TS)	No. 24 wire	1.108	0.315
	Subchannel 32	1.104	
Pin 406 (TW)	No. 25 wire	1.151	0.165
	Subchannel 30	1.149	
Pin 407 (TW)	No. 26 wire	1.100	0.224
	Subchannel 57	1.103	
Pin 408 (-)	No. 27 wire	1.102	0.411
	Subchannel 56	1.107	
Pin 409 (TS)	No. 28 wire	1.067	0.531
	Subchannel 55	1.073	
Pin 410 (-)	No. 29 wire	1.077	0.114
	Subchannel 73	1.075	
Pin 411 (TS)	No. 30 wire	1.013	0.630
	Subchannel 72	1.007	
Pin 412 (-)	No. 31 wire	0.989	0.356
	Subchannel 71	0.986	
Pin 413 (TW)	No. 32 wire	0.923	0.688
	Subchannel 70	0.916	
Pin 414 (TW)	No. 33 wire	0.994	0.384
	Subchannel 69	0.991	
Pin 415 (-)	No. 34 wire	1.035	0.430
	Subchannel 68	1.030	
Pin 416 (TW)	No. 35 wire	1.095	0.348
	Subchannel 67	1.091	
Pin 417 (TV)	No. 36 wire	1.099	0.269
	Subchannel 44	1.096	
Pin 418 (TW)	No. 37 wire	0.997	0.628
	Subchannel 42	1.003	

thicker. For sodium, the Prandtl number is very small, typically in the range of less than 0.01. This means that the conductive heat transfer mechanism dominates that of momentum transfer. Most turbulence models that rely on the concept of eddy diffusivity to describe turbulent heat transfer use turbulent Prandtl numbers.

Bricteux performed a numerical analysis of the flow characteristics of a liquid metal between two plates at a low Reynolds number using the LES and DNS methods [19]. Since the Reynolds analogy cannot be used for turbulent heat transfer in liquid metals, it is suggested that a different concept of the turbulent Prandtl number should be used [20]. For Reynolds analogy approaches, based on the similarity between momentum and heat diffusion, the turbulent Prandtl number ( $Pr_t$ ) has been proposed to model the turbulent heat flux. The Reynolds analogy is a commonly used approach to evaluate turbulent thermal diffusivity. This approach introduces a turbulent Prandtl number by assuming similarities in the turbulent transport of momentum and heat. In most cases, the turbulent Prandtl number is considered to have a constant value in the range of 0.8-1.0, and in most cases, it has been proposed through major assumptions without a physical basis. The

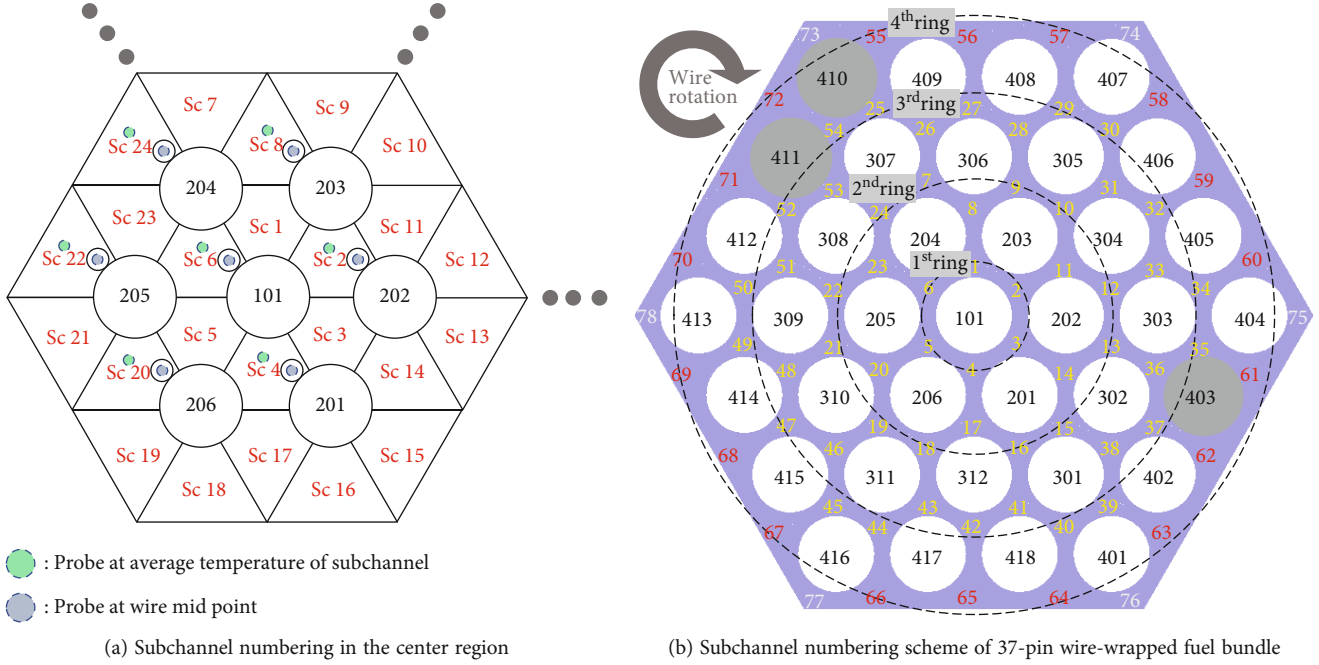


FIGURE 15: Comparison according to temperature measurement location (the temperature of the center point of the wire spacer is similar to the temperature of the subchannel in the adjacent area).

$Pr_t$  model is always used to calculate turbulent heat transfer because the turbulent eddy viscosity ( $\mu_t$ ) can be obtained in eddy viscosity models. As known from Equation (20),  $Pr_t$  is defined as the ratio of the momentum eddy diffusivity to the thermal eddy diffusivity [20].

$$Pr_t = \frac{\epsilon_m}{\epsilon_h} \quad (20)$$

Eddy viscosity models are based on the analogy between the molecular gradient-diffusion process and turbulent motion. The concept of a turbulent eddy viscosity  $\mu_t$  makes it possible to model the stress tensor as a function of mean flow quantities. The eddy viscosity models in Simcenter STAR-CCM+ solve additional transport equations for scalar quantities from which the turbulent viscosity  $\mu_t$  can be derived [16]. The turbulent mixing energy  $k$  and the specific dissipation rate  $\omega$  are required to define the eddy  $\mu_t$  [21]. In  $k - \omega$  turbulence models, the turbulent eddy viscosity  $\mu_t$  is calculated as

$$\mu_t = \alpha^* \frac{\rho k}{\omega}. \quad (21)$$

In Wilcox's model, the closure constants are determined as  $\alpha^* = 1.0$  [21].

The effective viscosity, which is composed of both laminar and turbulent viscosity, is calculated as follows:

$$\mu_{\text{eff}} = \mu + \mu_t. \quad (22)$$

The effect of turbulent flow, through turbulent eddy viscosity, induces enhanced heat transfer in the energy transport

equation. Therefore, this enhancement can take into account the effective thermal conductivity due to turbulent flow.

$$\lambda_{\text{eff}} = \lambda + \frac{\mu_t C_p}{Pr_t}. \quad (23)$$

For RANS turbulence models, the energy transport equation can be written as [16]

$$\frac{\partial}{\partial t} (\rho \bar{E}) + \nabla \cdot (\rho \bar{E} \bar{\mathbf{v}}) = -\nabla \cdot \bar{\mathbf{p}}_{\text{mod}} \bar{\mathbf{v}} + \nabla \cdot (\bar{\mathbf{T}} + \mathbf{T}_{\text{RANS}}) \bar{\mathbf{v}} - \nabla \cdot \bar{\mathbf{q}} + \mathbf{f}_b \bar{\mathbf{v}}. \quad (24)$$

For RANS turbulence models, the definition of the mean heat flux in the energy equation is based on a Boussinesq approximation. By default, the mean heat flux  $\bar{\mathbf{q}}$  in the energy Equation (25) is assumed to be proportional to the turbulent eddy viscosity and inversely proportional to  $Pr_t$  as [16]

$$\bar{\mathbf{q}} = - \left( \lambda + \frac{\mu_t C_p}{Pr_t} \right) \nabla \bar{T} = -\lambda_{\text{eff}} \cdot \nabla \bar{T}. \quad (25)$$

$\mu_t$  is the turbulent eddy viscosity as given by the respective turbulence model and transport equations, and  $Pr_t$  is constant value. The  $\mu_t$  calculated as in Equation (21) affects the generation of turbulent kinetic energy in Equations (9), (10), (11), and (12), and its effect on turbulent heat transfer can be controlled by the user-defined  $Pr_t$  value. To accurately predict the turbulent heat transfer for a specific turbulence model and flow conditions in a given geometry, it is necessary to perform a sensitivity analysis on  $Pr_t$ . Therefore, a study was conducted to investigate the effect of changes in the turbulent

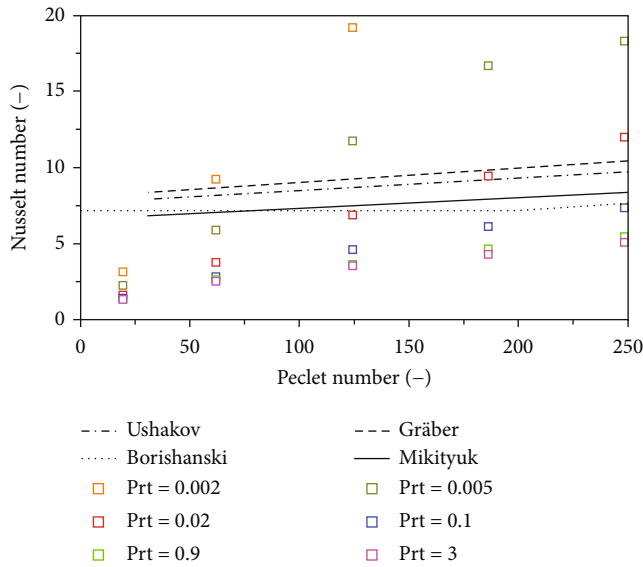


FIGURE 16: Heat transfer comparison of correlations and CFD results for different turbulent Prandtl numbers and a range of Peclet numbers.

Prandtl number on turbulent heat flux. The turbulent Prandtl number for a wire-wrapped fuel bundle was proposed using CFD by comparing it with the experimental result.

In this study, the global average Nusselt number defined by the Equation (26) was used for comparison with the heat transfer correlation.

$$Nu = \frac{hD_h}{\lambda} = \frac{q'' \cdot D_h}{\lambda \cdot (T_w - T_b)}. \quad (26)$$

When defining the Nusselt number, the global averaged values can differ significantly from the local values, which are very sensitive to the relative position in the bundle. Considering these two different approaches (global versus local), more reasonable and informed comparisons can be made to the existing empirical heat transfer correlations [22]. The global average Nusselt numbers from the NACIE and THEADES experiments are presented by Pacio et al. [23]. Figure 16 compares the heat transfer of correlation and CFD results for different Peclet numbers. The analysis results with turbulent Prandtl numbers in the range of 0.002 to 3 were compared with the liquid metal heat transfer correlations of Mikityuk [24], Ushakov et al. [25], and Gräber and Riger [26].

The Mikityuk correlation [24]

$$Nu = 0.047 \left( 1 - e^{-3.8((P/D)-1)} \right) (Pe^{0.77} + 250). \quad (27)$$

The Ushakov correlation [25]

$$Nu = 7.55 \left( \frac{P}{D} \right) - \frac{20}{(P/D)^{13}} + \frac{0.041}{(P/D)^2} Pe^{0.56+0.19(P/D)}. \quad (28)$$

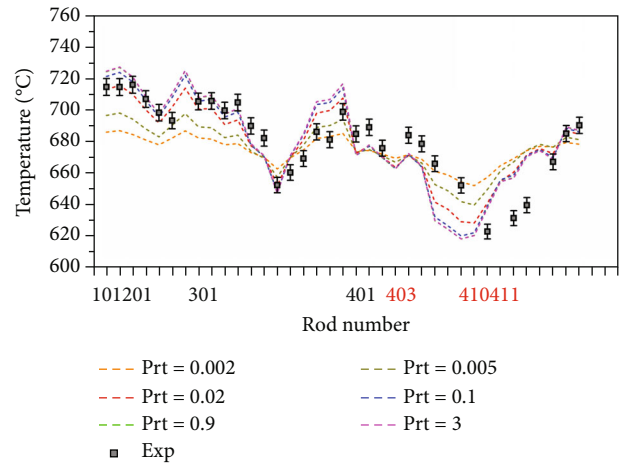


FIGURE 17: Comparison of experimental results with CFD results for different turbulent Prandtl numbers.

The Gräber correlation [26]

$$Nu = 0.25 + 6.2 \left( \frac{P}{D} \right) + \left( 0.032 \left( \frac{P}{D} \right) - 0.007 \right) Pe^{0.8-0.024(P/D)}. \quad (29)$$

All three correlations could be used over the entire region of data ( $P/D = 1.1 - 1.95$  and  $Pe 30 - 5000$ ) [24].

These correlations were derived from data on tube bundles, not wire-wrapped rod bundles. The correlation equation does not include a variable for wire spacer geometry. Understanding the thermo-hydraulic behavior of bare rod bundles is a good approach to simulating heat transfer in the core of a nuclear reactor, but caution should be exercised when applying it to wire-wrapped rod bundles [27]. In this work, empirical correlations of the type given by Equation (26) are used to compare results, despite the fact that these models do not take into consideration phenomena such as overall swirl and flow recirculation behind the wires [23]. Since the presence of spacers has a tendency to increase heat transfer and pressure drop, these correlations can be considered conservative for actual fuel assemblies [28]. Therefore, a comparison of the Nusselt number was performed to observe the trends in the CFD analysis results.

A decrease in the turbulent Prandtl number leads to an increase in the Nusselt number, i.e. an increase in heat transfer. At the steady state velocity of 0.3407 m/s, the Peclet number is approximately 18.5 and there is no corresponding heat transfer correlation in this state.

Figure 17 compares the CFD results for different  $Pr_t$  numbers with the experimental results. An error bar considering the uncertainty of the thermocouple was displayed along with the experimental data. In addition to the insufficiencies of the measurement system, the measured values are inaccurate because the installed thermocouples have a tolerance of 0.75% level (maximum error  $\pm 7.5^\circ\text{C}$  at  $1000^\circ\text{C}$ ) and the quality of the thermocouples deteriorates beyond the allowable temperature range of up to  $600^\circ\text{C}$  [29]. The temperature distribution in the radial direction varies depending on the  $Pr_t$  number, which is significantly different at 0.002,

0.005, 0.02, and 0.1 (or 0.9, 3). In the central part (2nd ring, 3rd ring), where unheated pins have no effect, when  $Pr_t$  is large, there is less heat transfer takes place in the circumferential direction, thus the temperature appears high. On the other hand, when  $Pr_t$  is small, the temperature at the center is low, and the temperature of the 4th ring, which includes the unheated pins, is high. This difference in temperature distribution was particularly large at pins 407, 408, 409, 410, and 411. The reason is that the flow rate and temperature distribution of subchannel numbers 71, 72, 73, 55, 56, 57, and 74 were affected as the wire rotated clockwise. This means that, despite the low flow conditions with a low Peclet number, heat transfer to the relatively cold fluid around the unheated pin is effective due to the hot sodium in the center because of the high thermal conductivity of sodium. Furthermore, as  $Pr_t$  decreases, according to Equation (25), the turbulent heat flux increases, which enhances the turbulent heat transfer and reduces the temperature gradient.

Figure 18 shows the temperature contour at the top of the heated section for different  $Pr_t$ . The turbulent thermal diffusivity is proportional to the temperature gradient by the ratio of the turbulent viscosity to  $Pr_t$ . As  $Pr_t$  becomes smaller, the influence of the thermal diffusivity increases, and the temperature distribution in the radial direction tends to flatten. In Figure 18, the radial temperature distribution according to the change in  $Pr_t$  can be confirmed. These results are similar to those for the Nusselt number in Figure 16.

In Figure 17, the relative error between the CFD result and the experimental result is calculated and then averaged to be 2.32%, 1.95%, 1.63%, 2.36%, 2.54%, and 2.54%, respectively. The experimental temperature data is not an absolute value due to various uncertainties. Because of the limited information of the sodium experiment, there are also uncertainties in the CFD analysis, so this sensitivity analysis was performed to compare the trend with the experimental data. In the cases shown in Figure 16, the effect of the temperature gradient due to  $Pr_t$  was found to be minimal when  $Pr_t$  is greater than 0.9. This is because the present case corresponds to a low Reynolds number flow with a very small Peclet number. As  $Pe$  increases, the proportion of heat transfer dominated by conduction decreases and the influence of convection increases, resulting in differences in heat transfer phenomena due to changes in  $Pr_t$ . 0.02 was used for  $Pr_t$  in this CFD analysis, which is consistent with the results for  $Pr_t$  previously obtained by Jeong et al. for a SIENA 7-pin fuel assembly [3]. However, the values for  $Pr_t$  determined in these experiments are not generally applicable and are only applicable to the PLADNTL 37-pin fuel bundle. Therefore, it is necessary to define this part as a limitation of the turbulence model application and further verification is needed to evaluate the suitability of the turbulence model application in the future. Further research is needed on different wire-wrapped fuel bundle geometries, uncertainties in sodium thermal conductivity, uncertainties in turbulent flow, uncertainties in heating conditions, and various flow regime etc.

**4.2. Validation of Experimental and CFD Results for the Steady State.** In this study, the results for the steady state were verified before an LOF event occurred. As shown in

Figure 2, to compare the results in each radial direction, the ring number was assigned according to the position of the pin, and each numbered ring was analyzed. Furthermore, the temperatures at points A to F, which are the positions of the duct wall surfaces, were also compared. Since pin numbers 206, 404, 408, 410, 412, and 415 marked in red are positions where the temperature is not provided, the temperatures at the other positions are compared. Figure 19 shows the temperature distribution of the numerical study obtained using STAR-CCM+ and the experimental data. As mentioned earlier, the experimental values are shown with an error of 0.75%. Since the PNC report only provides results for the top of the heated section, the comparison with this CFD analysis was made at the top of the heated section. Figure 19(a) shows the CFD and experimental temperature comparison for the 1st and 2nd rings; Figure 19(b) for the 3rd ring; Figure 19(c) for the 4th ring; and Figure 19(d) for the temperature at the duct wall. The temperature distributions in the 1st, 2nd, and 3rd rings were in good agreement with the experimental results. At pin 307 of the 3rd ring and pin 410 of the 4th ring, the temperature distribution calculated using CFD crosses over the experimental result.

This part is located along the periphery adjacent to the two unheated pins 410 and 411. Similarly, the temperature distribution of the duct wall surface at edges D and E around the unheated pin was overestimated compared to the experimental results. CFD overestimated the temperature distribution around the unheated pin, which seems to be due to the difference in the flow distribution of the subchannel because the mixing effect of the wire spacer is different from the actual one. In the corner and edge subchannels near the wall of the duct, the prediction of the temperature and mass flow in experiments and CFD tends to be inaccurate. In Figure 19(c), the regions where experimental errors often occur are all near the corner and edge subchannels. When the wire spacer of the pins in the 4th ring does not belong to the edge and corner subchannels, the difference between the experimental result and the CFD result is relatively smaller than that of other pins that belong to the edge and corner subchannels. The relative error is defined as in Equation (30), and the maximum relative error of 5% occurs at pin 414.

$$\text{Relative error} = \left| \frac{T_{\text{EXP}} - T_{\text{CFD}}}{T_{\text{EXP}}} \right| \times 100\%. \quad (30)$$

**4.3. Effect of Radial Temperature Difference with Number of Heated Pins.** Kabir and Hayafune noted that the presence of three unheated pins within the fuel pin bundle had a significant effect on the radial temperature distribution [2]. In addition, it was mentioned that after boiling occurred in the central part, an uneven radial temperature distribution was generated by the three unheated pins, thereby increasing the boiling area eccentrically. In contrast to the experimental report, which presents the results only after boiling, in this section, we present an analysis of the effect of the unheated pin on the radial temperature distribution before boiling. In other words, we have considered the skewing effect of the radial pin power. The skewing effect of this radial pin power has also been



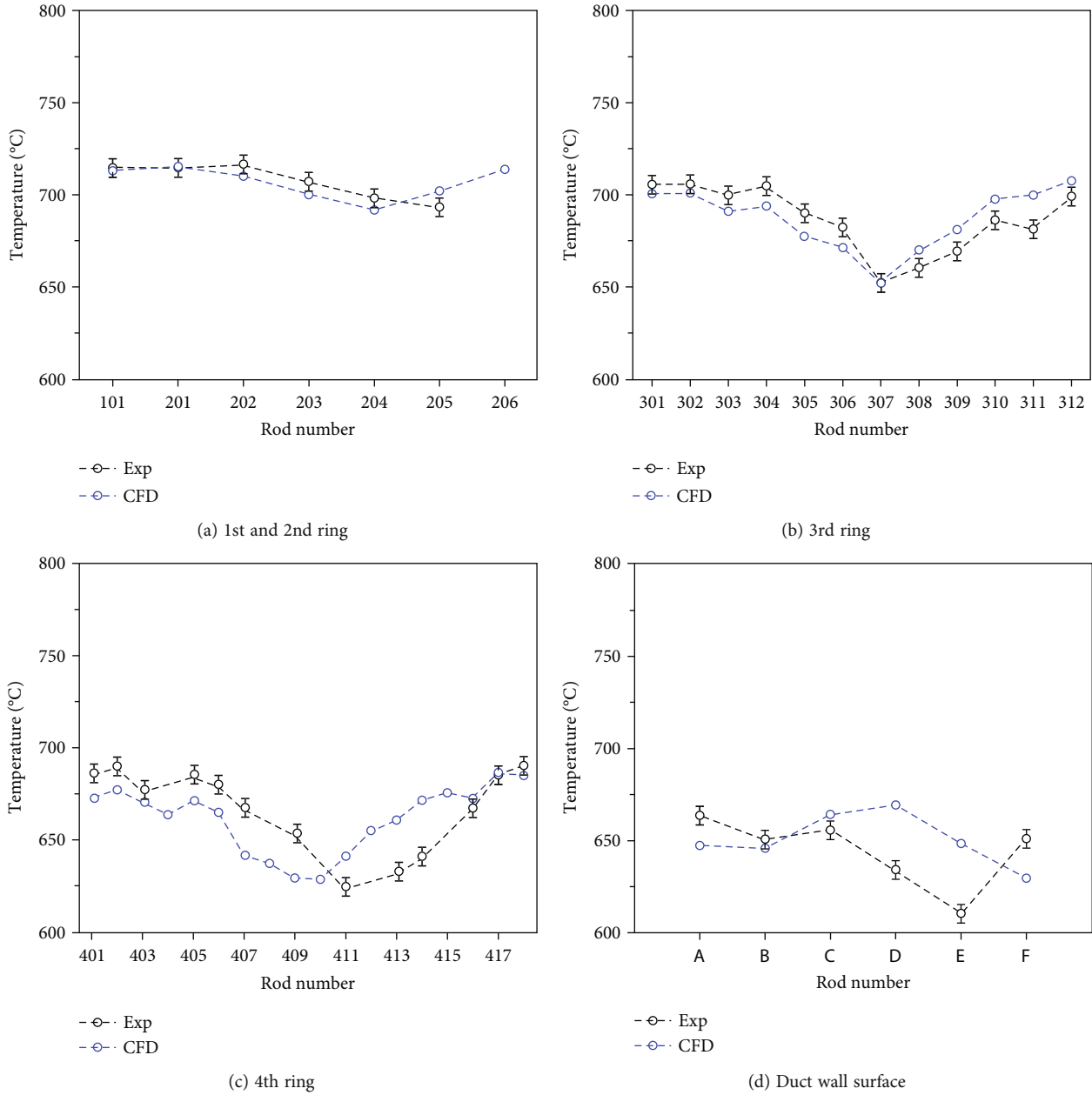


FIGURE 19: Comparison of experimental results and CFD analysis results for the top of the heated section in the steady state.

- (1) To determine temperature profiles in a simulated segment of an FTR fuel subassembly near the wrapper with a linear power skew factor
  - (2) To determine mixing effects in a simulated segment of an FTR fuel subassembly by heating the centrally located seven heater pins
  - (3) To further investigate the effect of wire-wrap sweeping on hexagonal duct temperatures
  - (4) To investigate the steep power gradient at low power levels and low flows expected in the LMFBR demonstration reactor blanket
  - (5) To impose a 3/1 power skew on the bundle to exaggerate temperature differences across the bundle and across the hexagonal flats to further investigate temperature anomalies seen in  $\pm 10\%$  power skew runs
- As such, researches have been conducted to understand the temperature gradient caused by the radial pin peaking factor, and in this study, we also conducted an additional study to understand the effect of radial temperature distribution as mentioned by Kabir and Hayafune.
- The flow area inside the duct was compared along the  $x$ -axis. When viewed from the top of the heated section in the  $+z$ -axis perspective, the analysis was performed in the clockwise direction. The power of the pins for each case is listed in Table 8.

TABLE 8: Radial power skew with difference the number of heated pins.

Parameter	34 heated pins	37 heated pins
Total power	100 kW	
Power of each pin	Total power/34 (without pin 403, 410, 411)	Total power/37 (all pins)
Axial power distribution	$Q_z = 0.9929704 \times \cos(0.0223841(z - 46.5)) + 0.007079315$	

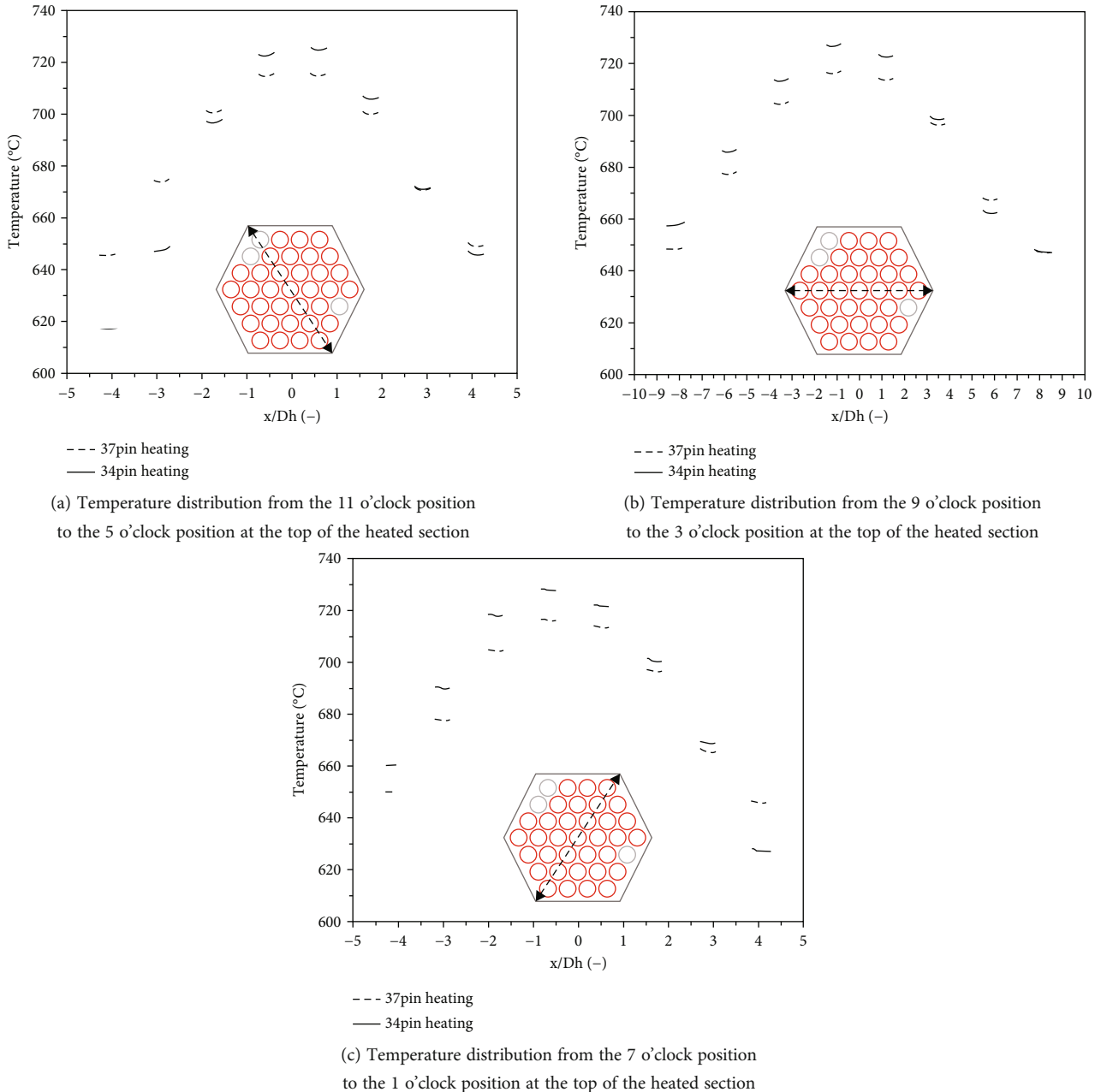


FIGURE 20: Effect of radial temperature distribution by the number of heated pins at the top of the heated section (dotted and solid lines indicate the heating conditions for 37 and 34 pins, respectively).

Only the number of pins to be heated is different, but the axial power distribution ( $Q_z$ ) is the same. For the same amount of total power, because only 34 pins are heated, 1.088 times more power is applied to each pin than when all pins are heated. Therefore, in the central region, where the effect of the unheated

pin is less, the temperature of the sodium appears high because it is affected by the greater amount of power. Figure 20 shows the difference when the same 100 kW power is applied to 37 pins compared to 34 pins. The dotted and solid lines represent 37-pin and 34-pin heating conditions, respectively. These

TABLE 9: Temperature difference in each heating case according to the measurement line.

Temperature measurement line	From 11 o'clock position to 5 o'clock position		From 9 o'clock position to 3 o'clock position		From 7 o'clock position to 1 o'clock position	
	34pin	37pin	34pin	37pin	34pin	37pin
Maximum temperature (°C)	728.5	716.7	728.1	716.9	728.6	716.8
Minimum temperature (°C)	615.9	645.5	647	647.3	627.4	645.7
Max-min (°C)	112.6	71.2	81.1	69.6	101.2	71.1

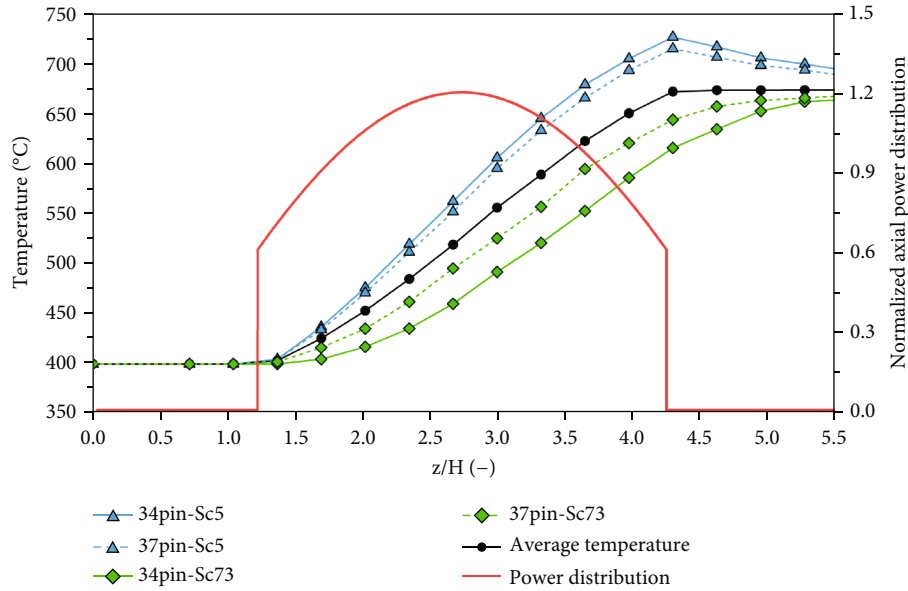


FIGURE 21: Comparison of subchannel and average sodium temperature along the z-axis.

results can be inferred by observing the temperature distribution of the line that crosses (a) from the upper left to the lower right of the duct (11 o'clock to 5 o'clock), (b) from the left end to the right end of the duct (9 o'clock to 3 o'clock) and (c) from the lower left to the upper right of the duct (1 o'clock to 7 o'clock). The effect of the unheated pin can be seen through the temperature distribution of each line. If the dotted line has a higher temperature than the solid line, it means that the unheated pin has a large effect on that area. If the unheated pins have an effect, it is because the relatively cold fluid around them flows into the surrounding subchannel. Figure 20(a) compares the temperature distribution of the line from the top left to the bottom right, where the effect of the unheated pin is greatest. In the top left corner of subchannel 73, interior subchannel 54, and the surrounding areas, the effect of the unheated pin was particularly significant. The temperature in the upper left corner is low because of the two unheated pins. In Figure 20(b), the temperature difference between the solid and dotted lines is the largest in the central region; the solid line temperature is higher in the left end region; and the dotted line temperature is slightly higher at subchannels 34 and 35. The reason for this distribution is that the effect of the unheated pin is small in the central region. Furthermore, in the region on the left, the effect of the unheated pin is small, and the orientation of the wire is such that it rotates clockwise, in which case the convective heat diffusion around pin 413

would not have been significantly affected. This is because pin 413 is moving away from pins 410 and 411 in a counter-clockwise direction. At the right end, the effect of the unheated pin was slightly dominant due to the influence of pin 403 below. In Figure 20(c), the region where the effect of the unheated pin is noticeable is the upper right region, and corner subchannel number 74 was most affected. This is because convective diffusion often occurs between edge or corner subchannels within the same ring. As shown in Figure 20, for areas that are greatly affected by unheated pins (when only 34 pins are heated), the temperature distribution in the radial direction has a large deviation. Table 9 shows the difference between the maximum and minimum temperatures according to each temperature measurement location. At all measurement locations, when only 34 pins were heated, the temperature deviation was greater than when all 37 pins were heated. This means that the radial power skew had a significant effect on the radial temperature distribution. In the case with the largest temperature deviation shown in Figure 20(a), the lowest temperature was measured in subchannel 74, and the highest temperature was measured in subchannels 3 and 4.

In addition, the temperature changes along the z-axis of subchannel 5, one of the interior subchannels, and along subchannel 73, one of the corner subchannels, are compared in Figure 21. The normalized axial power distribution and the average sodium temperature of each plane along the z

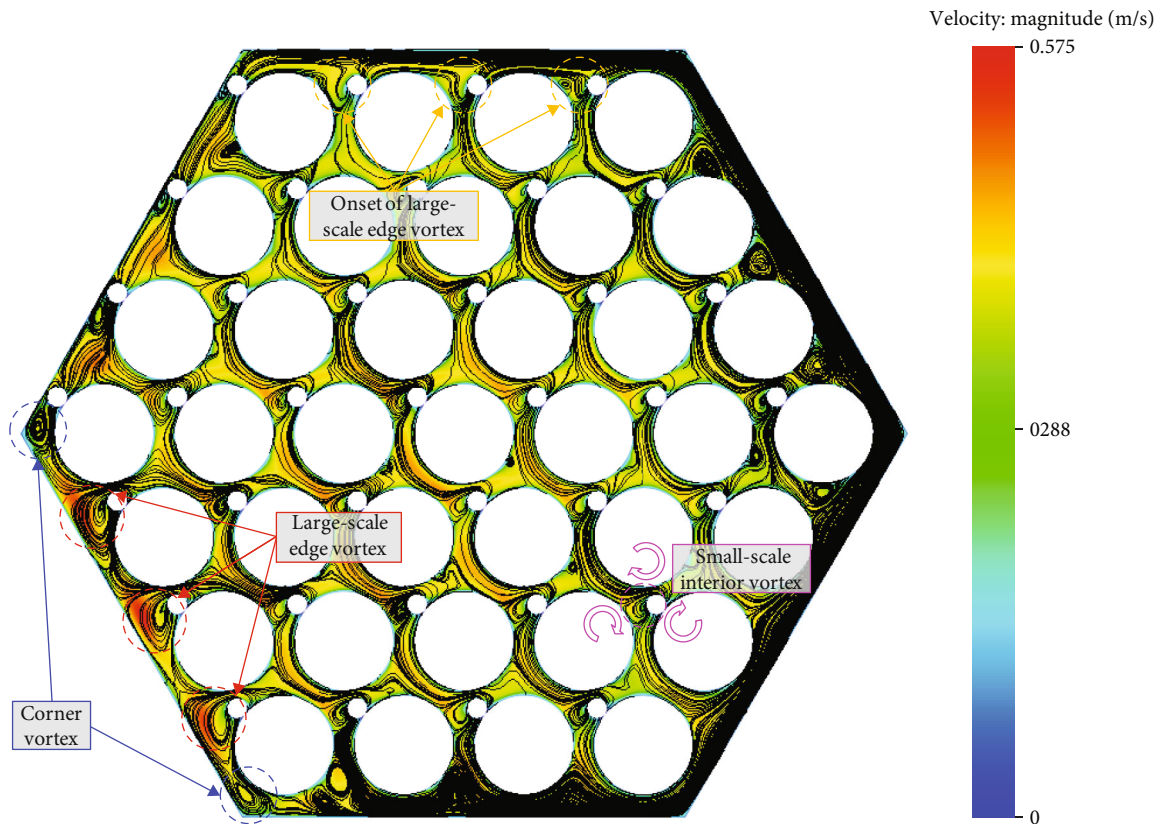


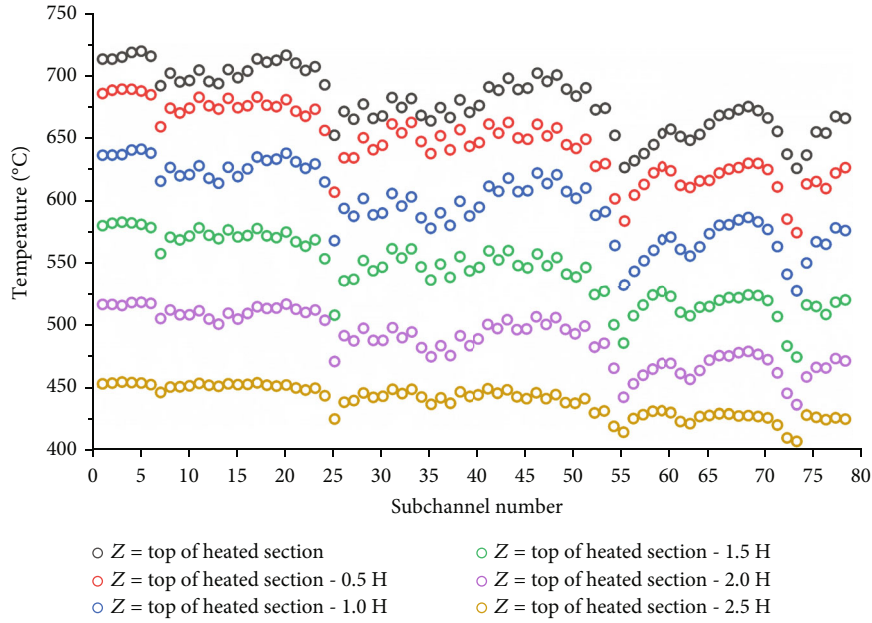
FIGURE 22: Vorticity and velocity contours at the top of the heated section.

-axis are also plotted. As in the heated region in Figure 4, a chopped cosine axial power distribution is applied to a length of 930 mm. In the interior subchannel, the temperature is higher than the average surface temperature due to the effect of more power and less mass flow. On the other hand, in the corner and edge subchannel, the temperature is lower than the average sodium temperature because it is less affected by the power and greater mass flow of the coolant. In addition, the walls of the duct are adiabatics and the flow resistance is low because the edge subchannels have a larger hydraulic diameter than the interior subchannels. Beyond the heated region, the temperature gradually decreases in the interior subchannel due to the mixing effect of the wire spacer, and the temperature in the corner subchannel gradually rises to approach the average temperature even once heating ceases. When 37 pins are heated, uniform power is applied to all pins, so the temperature of the corner and interior subchannels is relatively close to the average sodium temperature. On the other hand, when only 34 pins are heated, the temperature of the corner subchannel is low because of the effect of the unheated pins, and the temperature of the interior subchannel is high because it receives more power.

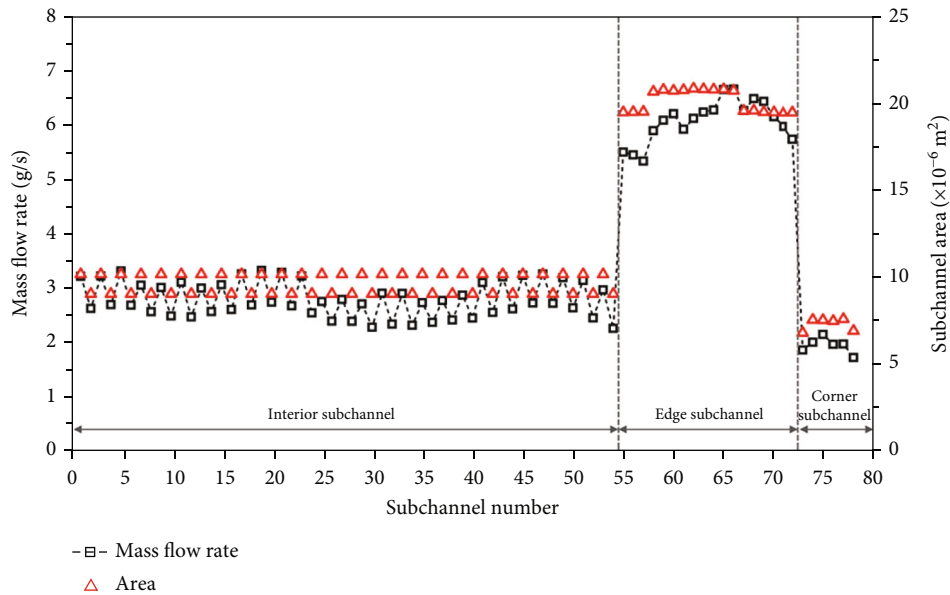
As shown in Figure 22, the relative position of the vortex in each subchannel is closely related to the vortex structure behavior and the three-dimensional flow phenomenon. The edge, corner, and interior vortex structures are periodically changed according to the relative positions of the wire spacer and the duct [4, 5, 33]. The edge vortex structure has

a larger axial velocity than other vortex structure, and the edge vortex structure is a type of longitudinal vortex and has a larger scale than other subchannels. The strong longitudinal vortex structure in the edge subchannel can achieve better heat transfer characteristics than in the corner and interior subchannels. The vortex structure affects the heat transfer characteristics.

**4.4. Analysis of Subchannel Temperature.** For effective V&V work with subchannel codes, it is important to provide subchannel information. In this section, the average temperature, mass flow rate, and area values of all 78 subchannels are provided. The mass flow and area information are provided for results related to the top of the heated section. The temperature data was measured for each height along the  $z$ -axis, and the temperature data is provided on the  $z$ -plane with a 0.5 wire lead pitch reduction from the top of the heated section to the bottom. Although the overall average temperature is the same even beyond the top of the heated section, the temperature distribution between the subchannels varies due to the thermal mixing effect of the wire spacer. The temperature was measured on a total of six planes, and the temperature data are colored as shown in Figure 23(a). The temperature is classified according to the ring number of the subchannel, as shown in Figure 15(b). Subchannels 25, 54, 55, 72, and 73, which are the regions most affected by the unheated pins, have a relatively lower temperature than the surrounding subchannels, and this trend is distributed over all positions on the  $z$ -plane.



(a) Average temperature of each subchannel along the z-axis (each temperature is compared on a surface reduced by 0.5 wire lead pitch to the top of the heated section)



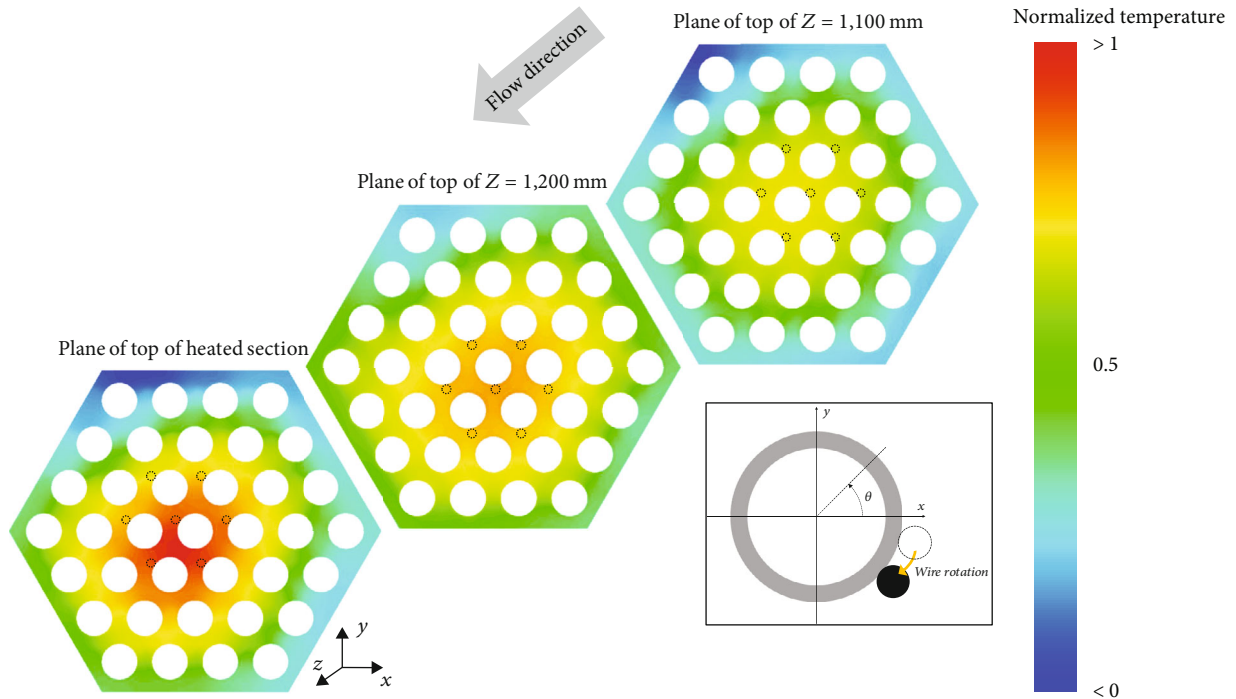
(b) Mass flow rate and cross-sectional area of subchannels at the top of the heated section

FIGURE 23: Comparison of temperature, mass flow rate, and area of subchannel at the top of the heated section.

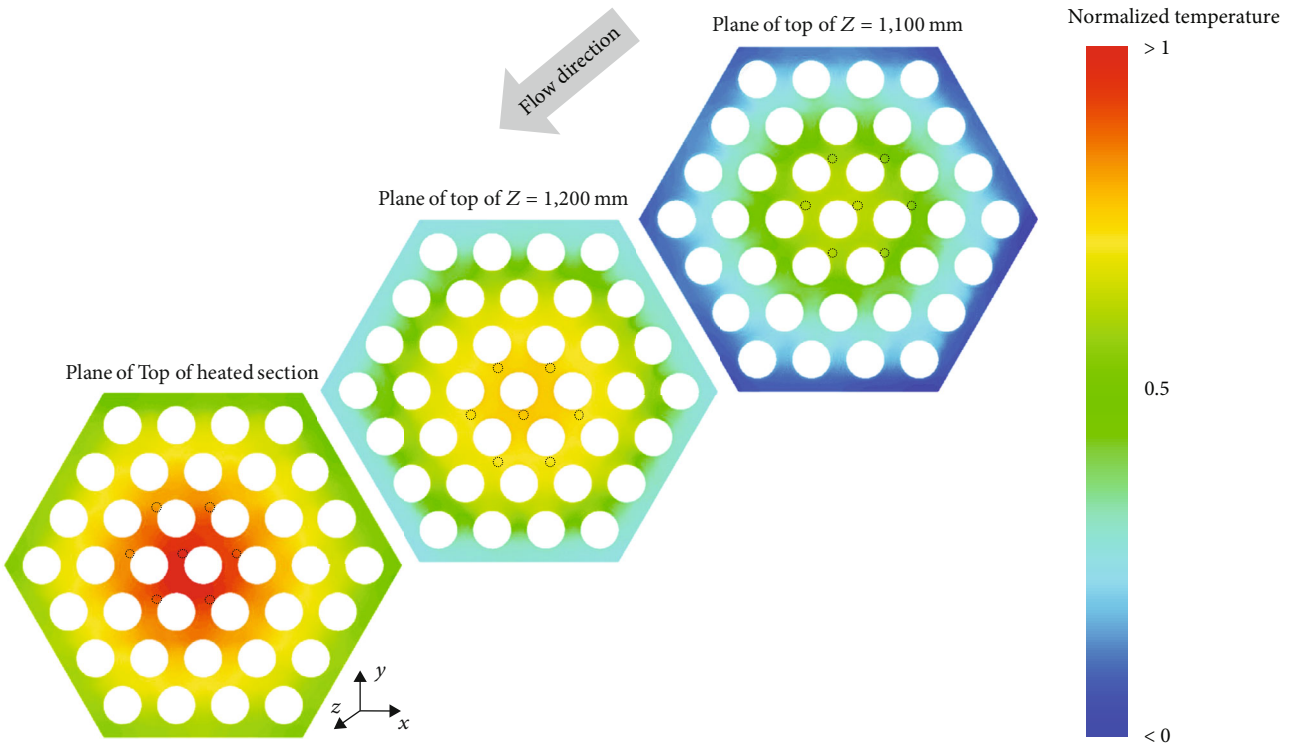
The maximum temperature occurs in the interior subchannel 5, and the minimum temperature occurs in the corner subchannel 73. Figure 23(b) shows the area and mass flow rate of each subchannel. Even in the same interior subchannel, the area of the subchannel changes depending on the relative position of the wire spacer. The area of the subchannel decreases as the area occupied by the wire decreases, and the mass flow rate decreases accordingly. Compared to the narrow interior or corner subchannels, the edge subchannel occupies a large area and thus accommodates a large mass flow.

Figure 24 shows the change in the temperature contour along the z-axis according to each heating condition. To sim-

plify the presentation of the temperature gradient, the contour does not include the heater section but only the fluid region, wire, and cladding sections. As in the analysis in the previous section, under 34-pin heating conditions, the temperature gradient of the edge, corner channel, and interior subchannels is mainly due to the effect of the unheated pins, and the temperature appears high in the regions far from the unheated pins. On the other hand, under 37-pin heating conditions, the temperature gradient of the edge, corner, and interior subchannels is small because the thermal mixing effect of the wire spacer is relatively large, and a uniform temperature distribution appears at the top of the heated section.



(a) Normalized temperature contour when 34 pins are heated

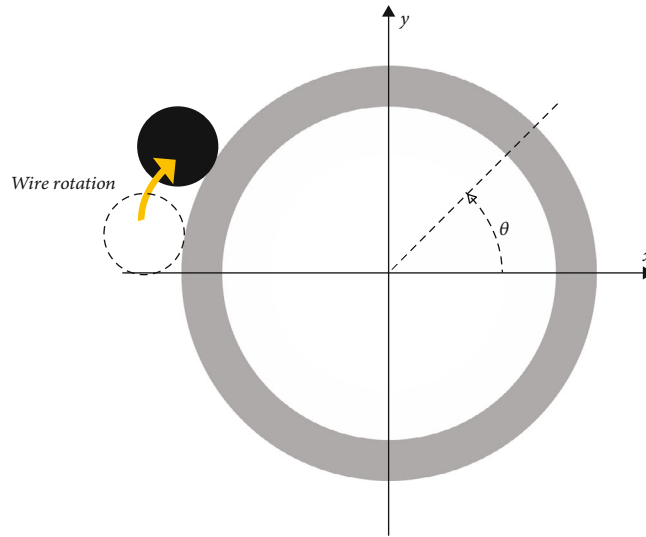


(b) Normalized temperature contour when 37 pins are heated

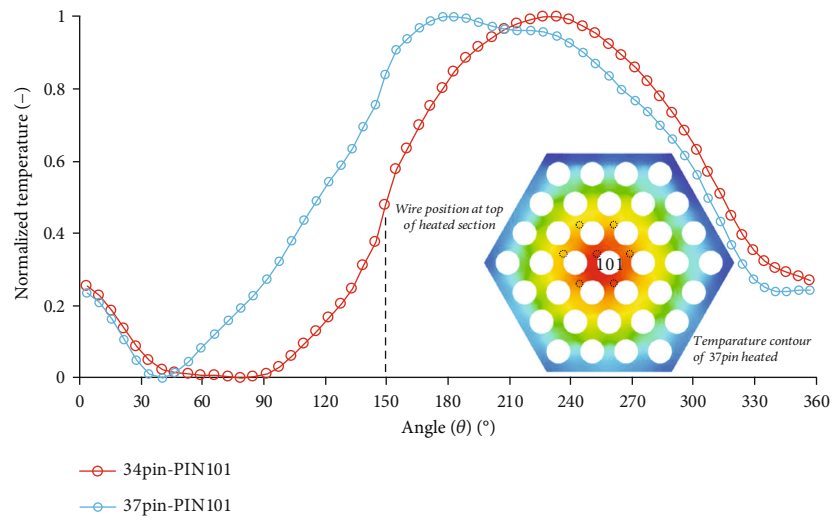
FIGURE 24: Difference in the temperature field according to the number of heated pins (The cross-section of the cladding and wire was included in the temperature contour).

4.5. Analysis of Pin Temperature with respect to Azimuth Angle. This section presents the analysis of the dependence of the temperature and peak temperature on the azimuth angle of the pin cross section. Evaluating the fuel rod tem-

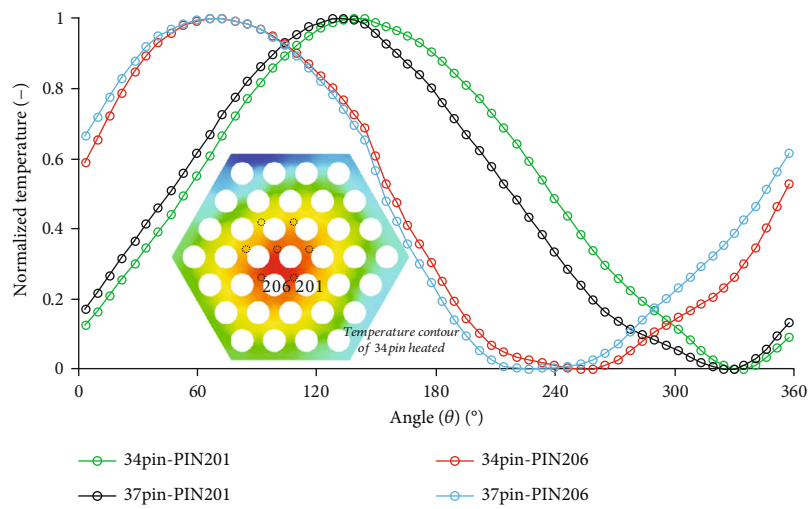
perature is one of the most important issues in reactor uncertainty analysis. Depending on the cladding peak temperature, the hot channel factor is defined and the reactor safety margin is designed. The cladding peak temperature



(a) Wire rotation direction and azimuth reference angle



(b) Pin 101



(c) Pins 201 and 206

FIGURE 25: Continued.

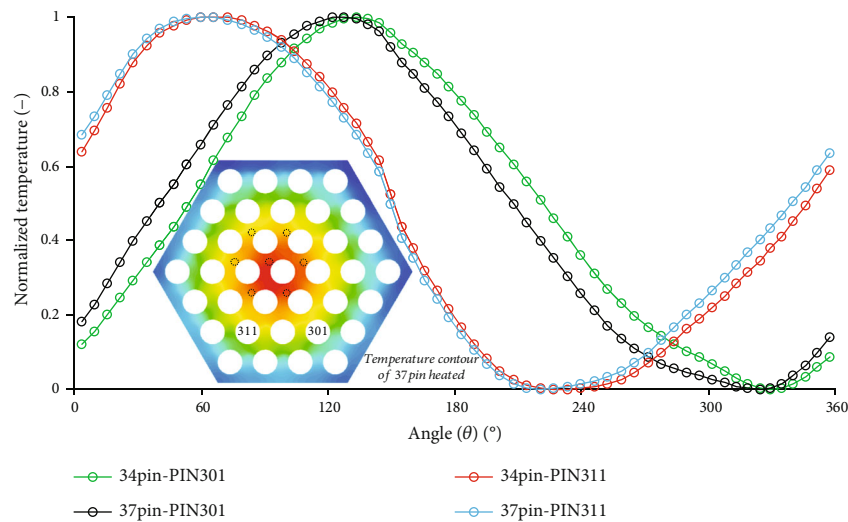
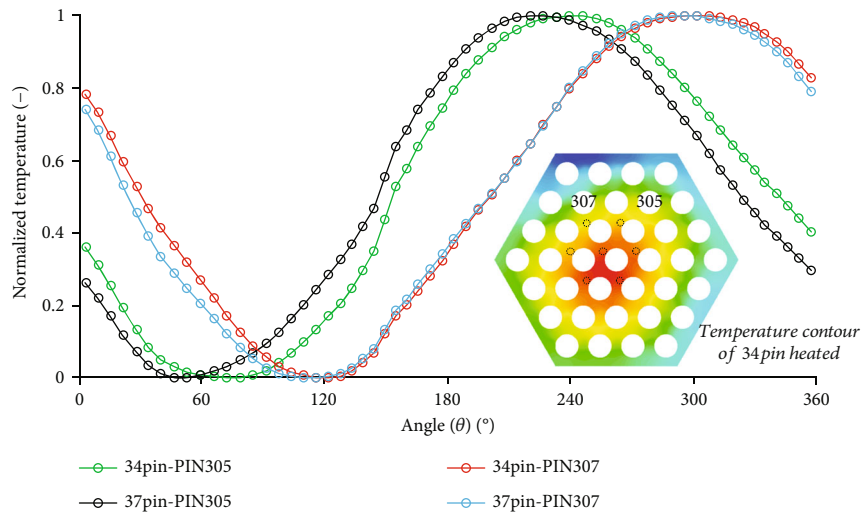
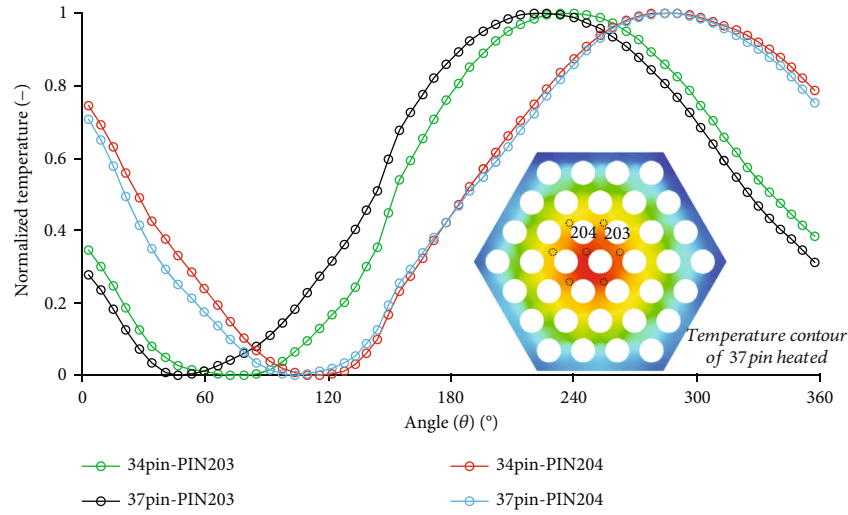


FIGURE 25: Continued.

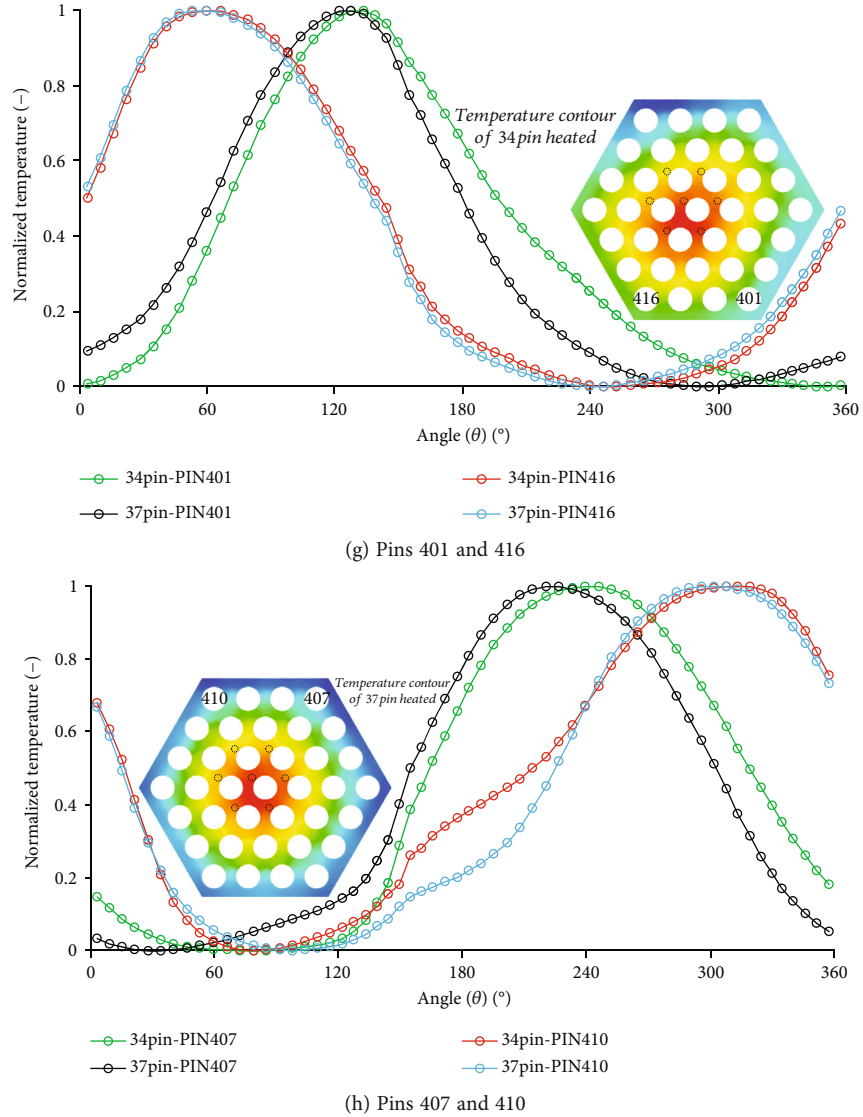


FIGURE 25: Comparison of azimuthal temperature for each pin (the temperature contour is normalized to the maximum and minimum temperatures. The columns (a, c, e, g) and (b, d, f, h) show the temperature contour when 34 and 37 pins are heated, respectively).

was analyzed by determining the temperature change as a function of the azimuth angle at the top of the heated section and the effect of the unheated pins on the peak temperature.

Figure 25 shows the top of the heated section to compare the temperature of pin numbers 101, 201, 203, 204, 206, 301, 305, 307, 311, 401, 407, 410, and 416. As shown in Figures 3(a) and 4, the position of the wire at the top of the heated section is directed at 150°, and the reference azimuth is selected as shown in Figure 25(a). The temperature was compared by defining the normalized temperature as in Equation (31). The normalized temperature is defined as the maximum and minimum temperatures of the pin, respectively.

$$T^* = \frac{T - T_{\min}}{T_{\max} - T_{\min}}. \quad (31)$$

For ease of comparison, the normalized temperature contour of 34 heating conditions is shown in the left column of

Figure 25, and the normalized temperature contour of 37 heating conditions is shown in the right column. The radial power skew for each heating condition is listed in Table 8. Table 10 summarizes the angle at which the maximum and minimum temperatures and peak temperatures of each pin occur. Most of the results have a sinusoidal shape with the maximum and minimum temperatures of one cycle. In addition, there are discontinuous points where the temperature rapidly decreases or rises, exist in the vicinity of 150°, which is the position where the wires are in contact. The detailed analysis of the temperature distribution according to the azimuth for each pin is as follows:

(1) *Pin 101*. Figure 25(b) shows the comparison of pin 101, which is located in the center of the 1st ring. The 34-pin and 37-pin heating conditions are shown in red and blue, respectively. Unlike the average temperature, the hot spot due to the presence of wires attached to the cladding is always a concern as it can lead to failure of the cladding material [34]. The cladding temperature in the azimuth

TABLE 10: Maximum and minimum temperature according to the azimuthal angle of each pin.

Pin number	Number of heated pin	Maximum temperature (°C)	Minimum temperature (°C)	Max-min (°C)	Angle of max temperature (°)
101	34 pins	717.0	711.0	6.0	226.9
	37 pins	707.5	704.6	2.9	183.4
201	34 pins	715.3	698.0	17.3	139.0
	37 pins	706.3	693.9	12.4	133.4
203	34 pins	710.8	693.4	17.4	239.7
	37 pins	704.8	690.9	13.9	220.5
204	34 pins	711.8	689.8	22.1	284.0
	37 pins	706.2	694.5	11.7	284.0
206	34 pins	716.9	709.7	7.2	66.1
	37 pins	707.2	697.9	9.3	66.1
301	34 pins	700.0	670.7	29.3	133.4
	37 pins	694.2	671.0	23.2	127.8
305	34 pins	692.9	664.9	28.0	239.7
	37 pins	690.9	668.7	22.2	220.5
307	34 pins	689.0	649.5	39.5	302.0
	37 pins	694.3	673.4	20.9	296.1
311	34 pins	709.4	688.2	21.2	66.1
	37 pins	697.5	676.3	21.1	59.7
401	34 pins	672.6	650.8	21.8	133.4
	37 pins	671.1	653.4	17.7	127.8
407	34 pins	664.1	634.1	30.0	239.7
	37 pins	668.5	650.2	18.3	220.5
410	34 pins	648.4	621.9	26.5	310.6
	37 pins	672.7	650.5	22.2	302.0
416	34 pins	687.5	664.6	22.9	59.7
	37 pins	675.9	654.3	21.6	59.7

angle of the center pin is shown as a polar graph in Figure 26. As shown in Table 10, the peak temperature points for the 34-pin and 37-pin heated conditions are different. There is a difference in peak temperature of about 9.5°C, and the peak temperature is located near the wake region. The thermal resistance of the cladding is low, so the temperature gradient inside the cladding is small, but there is a localized temperature increase at the contact between the wire and the cladding.

(i) 34-pin heating conditions: the difference between the maximum and minimum temperature is 6°C, and the position of the angle where the peak temperature appears is approximately 226.9°. As shown in Figure 27(a), due to the effect of the unheated pins, the peak temperature occurred on the far side rather than at the exact position of the wake region of the wire. The effect of the three unheated pins increased the temperature gradient, and the effect of the thermal mixing by the wire was relatively smaller

(ii) 37-pin heating conditions: the difference between the maximum and minimum temperature is 2.9°C, and the angle at which the maximum temperature appears is approximately 183.4°. This position coincides with the wake region of the wire as shown in Figure 27(b)

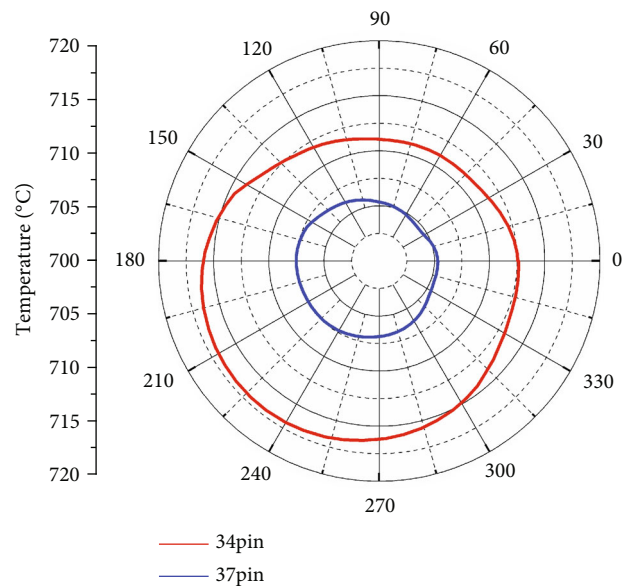


FIGURE 26: Polar graph of temperature according to the azimuthal angle of center pin.

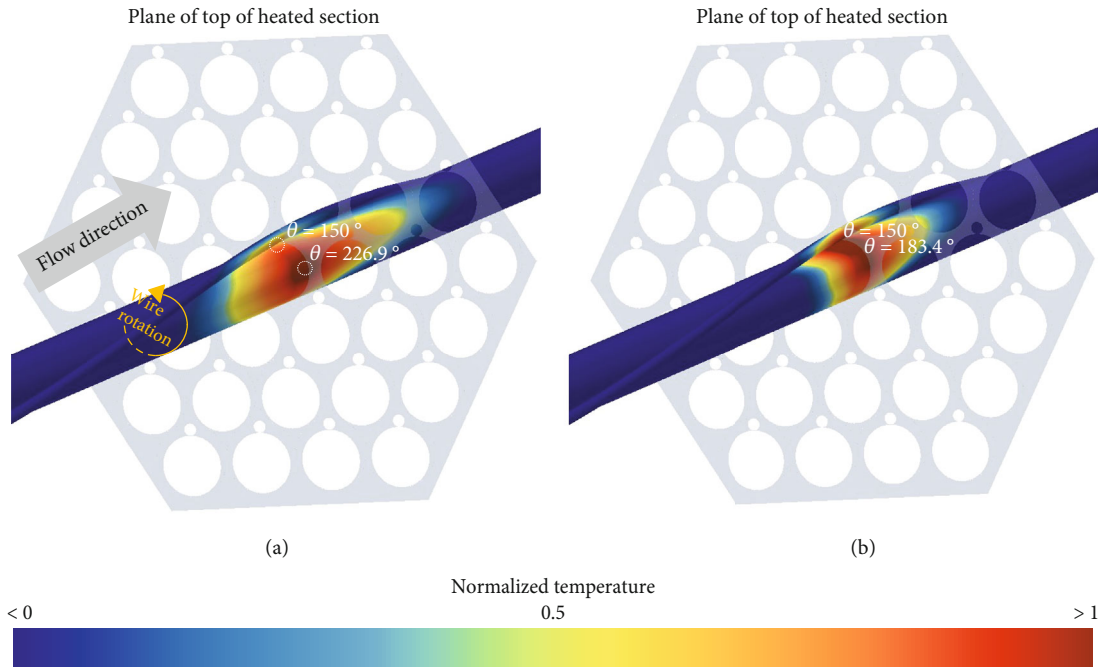


FIGURE 27: Temperature distribution of wire and cladding of pin 1 (the contour is normalized to the maximum and minimum temperature of each pin).

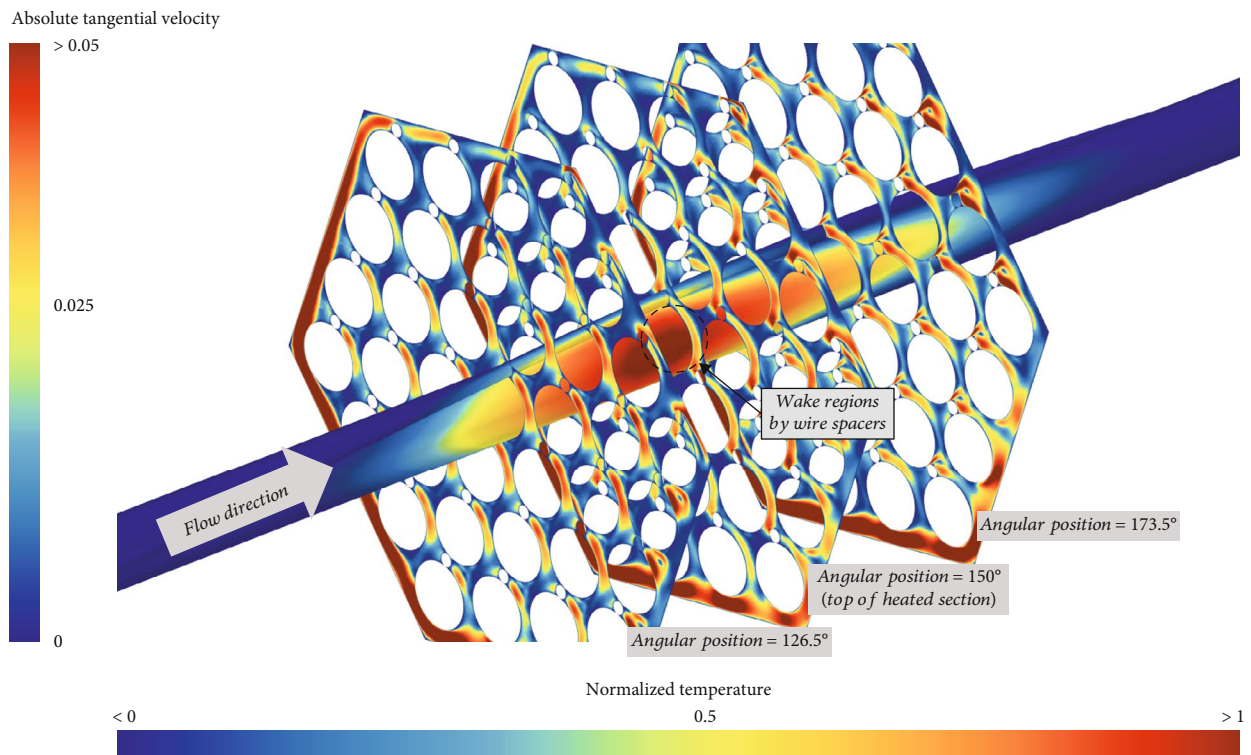


FIGURE 28: Tangential velocity distribution on the cross sectional planes (the colors of the pin and wire correspond to the legend of the normalized temperature).

Figure 28 shows the tangential velocity expressed as an absolute value. Referring to the angle of the top of the heated section shown in Figure 3, the tangential velocity was compared by adding two planes at the front and back. In the

interior subchannels, small-scale vortex structures develop between the wire-wrapped bundles. Locally, near the suction surface of wire spacers, wake regions develop due to helically wire spacers. The wire and transverse flow created a wake

with a low axial velocity region at the back of the wire. A low-velocity region appears behind the wire caused by the wake behind the wire [5].

(2) *Pins in the 2nd Ring.* Figures 25(c) and 25(d) compare the temperature distributions of pins 201, 203, 204, and 206, and these pins are located in the center adjacent to pin 101. The point where the peak temperature appears is located near pin 101, and the peak temperature of each pin appears with a phase difference of  $60^\circ$ . In the 34-pin heating condition, the largest temperature difference of  $22.1^\circ\text{C}$  occurred at pin 204. In addition, unlike the other pins, the minimum temperature of this pin was lower than the minimum temperature of the 37-pin heating condition compared to the 34-pin heating condition.

(3) *Pins in the 3rd Ring.* Figures 25(e) and 25(f) compare pins 301, 305, 307, and 311, and the position where the maximum temperature occurs for each pin is similar. The largest temperature difference of  $39.5^\circ\text{C}$  occurs at pin 307 under 34-pin heating conditions. Similar to the 2nd ring, a lower minimum temperature was generated due to the effect of the unheated pin, and the peak temperature was also lower than for the 37-pin heating condition.

(4) *Pins in the 4th Ring.* Figures 25(g) and 25(h) compare pins 401, 407, 410, and 416, and the position of the peak temperature for each pin is similar. The largest temperature difference of  $30.0^\circ\text{C}$  occurs at pin 407 under the 34-pin heating condition. The colder sodium of unheated pins 410 and 411 flowed through the edge subchannel and affected the temperature distribution of the subchannel around pin 407. The temperature along the edge and in the corner of the subchannel around pin 407 at  $78.9^\circ\text{C}$  is lower than that around the interior subchannel. Due to this effect, the lowest maximum and minimum temperatures occur at pin 410, which is an unheated pin, but the largest temperature difference occurs at pin 407.

## 5. Conclusion

In this study, the initial steady-state temperature data were verified by performing CFD analysis for the 37-pin wire-wrapped fuel bundle of the PLANDTL facility. A detailed description of the PLANDTL facility with reference to the PNC report is included. A hexahedral mesh was used to generate the same geometry as the test section of the 37-pin fuel bundle of the PLANDTL facility, and the following analyses were performed: axial grid sensitivity, radial grid sensitivity, turbulence model sensitivity, and turbulent Prandtl number.

The analysis of the 37-pin fuel assembly using the RANS-based STAR-CCM+ code was verified with the temperature data of the PLANDTL experimental facility. The results of the CFD investigation allowed the following conclusions to be made:

- (1) The CFD results were in good agreement with the friction factor correlation equations such as UCTD. The RANS model indicated no difference in the friction factor by each axial grid. The normalized velocity and TKE were compared according to the radial grid, and a difference occurred in the TKE value.

This is because the  $y^+$  value based on the wall-normal grid spacing directly influenced the calculation of the value of the specific dissipation rate in the  $k-\omega$  turbulence model

- (2) Two  $k-\varepsilon$  models and two  $k-\omega$  models were compared, and the normalized velocity and TKE were analyzed in the same way as above. With the  $k-\varepsilon$  model, the peak of the axial velocity is smaller than with the  $k-\omega$  model, and the maximum and minimum values of the TKE appear larger. The effect of this turbulence model also affected the difference in temperature distribution. The analysis showed that the temperature in the central region was lower and the temperature in the outer region was higher than with the  $k-\omega$  model due to the stronger turbulent kinetic energy of the  $k-\varepsilon$  model. A comparison of the friction factor with the UCTD showed that the two  $k-\omega$  models deviated from the UCTD by a small error, while the error of the  $k-\varepsilon$  model occurred at a low flow rate
- (3) As part of the heat transfer analysis, the  $Pr_t$  was analyzed. The heat transfer correlation according to  $Pr_t$  and the temperature distribution in the radial direction were compared. When  $Pr_t$  was 0.02, the heat transfer correlation and the temperature data of the experiment were the best. Therefore, the turbulent Prandtl number of the RANS analysis in this STAR-CCM+ code was analyzed using 0.02
- (4) The effect of an unheated pin on the temperature distribution of the surrounding subchannels was analyzed, and information on the temperature, mass flow rate, and area of each subchannel was provided. The temperature distribution of the coolant under 34-pin and 37-pin heating conditions was compared in the radial direction, and the temperature change along the  $z$ -axis of the interior subchannel and corner subchannel was analyzed. In addition, the analysis of the peak temperature and the dependence of its position on the azimuth angle for each pin allowed the region in which the peak temperature of the cladding of the wire-wrapped fuel bundle appeared to be investigated
- (5) The CFD analysis results calculated using the SST  $k-\omega$  model were compared with the experimental results measured at the top of the heated section. Only 31 pins with experimental temperature data were compared among pins 1 to 37, and the experimental result and CFD results were in good agreement within 5% of the relative error. Edge subchannels and corner subchannels had large errors, while interior subchannels showed relatively small errors

By successfully simulating the test section, the steady-state CFD results were in agreement with the experimental

results, and the transient analysis simulating the LOF event will be performed based on these results.

## Nomenclature

RANS:	Reynolds-averaged Navier-Stokes
$P$ :	Rod pitch
$D$ :	Rod diameter
$D_w$ :	Wire diameter
$H$ :	Wire axial pitch
$D_h$ :	Hydraulic diameter
$N_r$ :	Number of pins in the bundle
$Pr$ :	Prandtl number
$Pr_t$ :	Turbulent Prandtl number
$Nu$ :	Nusselt number
$Pe$ :	Peclet number
$Re$ :	Reynolds number
$Re_L$ :	Laminar to transition boundary Reynolds number
$Re_T$ :	Transition to turbulent boundary Reynolds number
TKE:	Turbulent kinetic energy
$\epsilon_m$ :	Momentum eddy diffusivity
$\epsilon_h$ :	Thermal eddy diffusivity
$T$ :	Temperature
$\Theta$ :	Normalized temperature
$\lambda$ :	Thermal conductivity
$C_p$ :	Specific heat
$f$ :	Friction factor
$v$ :	Velocity
$p$ :	Pressure
$k$ :	Turbulent kinetic energy
$\rho$ :	Density
$\mu$ :	Dynamic viscosity
$\epsilon$ :	Dissipation rate of $k$
$\omega$ :	Specific dissipation rate of $k$
$\mu_t$ :	Turbulent eddy viscosity
$\mu_{\text{eff}}$ :	Effective eddy viscosity
$\lambda_{\text{eff}}$ :	Effective thermal conductivity
$\bar{q}$ :	Mean heat flux
$h$ :	Heat transfer coefficient
$q''$ :	Heat flux
$T_w$ :	Wall temperature
$T_b$ :	Bulk temperature.

## Data Availability

The data used to support the findings of this study are included within the article.

## Conflicts of Interest

The authors declare that there are no conflicts of interest regarding the publication of this paper.

## Acknowledgments

This work was supported by a Korea Institute of Energy Technology Evaluation and Planning (KETEP) grant funded by the Korean government (MOTIE) (No. 20214000000780, Methodology Development of High-fidelity Computational

Fluid Dynamics for next generation nuclear power). This work was additionally supported by a National Research Foundation of Korea (NRF) grant funded by the Korea government (MSIT) (No. 2021M2E2A2081062). This work was supported by the Korea Institute of Energy Technology Evaluation and Planning (KETEP) grant funded by the Korea government (MOTIE) (RS-2023-00243201, Global Talent Development project for Advanced SMR Core Computational Analysis Technology Development). This research made use of the resources of the High Performance Computing Center at Idaho National Laboratory, which is supported by the Office of Nuclear Energy of the U.S. Department of Energy and the Nuclear Science User Facilities under Contract No. DE-AC07-05ID14517.

## References

- [1] Nuclear Energy Agency, *Computational fluid dynamics for nuclear reactor safety applications-6 (CFD4NRS-6)*, Committee ON the Safety of Nuclear Installations, NEA/CSNI/R, 2017.
- [2] M. E. Kabir and H. Hayafune, *Study of thermohydraulic behavior within the fuel bundle under a loss of flow condition*, Power Reactor and Nuclear Fuel Development Corporation, PNC TN9410 92-018, 1992.
- [3] J.-H. Jeong, M.-S. Song, and K.-L. Lee, "Thermal-hydraulic effect of wire spacer in a wire-wrapped fuel bundles for SFR," *Nuclear Engineering and Design*, vol. 320, pp. 28–43, 2017.
- [4] J.-H. Jeong, M.-S. Song, and K.-L. Lee, "RANS based CFD methodology for a real scale 217-pin wire-wrapped fuel assembly of KAERI PGSFR," *Nuclear Engineering and Design*, vol. 313, pp. 470–485, 2017.
- [5] M.-S. Song, J.-H. Jeong, and E. S. Kim, "Numerical investigation on vortex behavior in wire-wrapped fuel assembly for a sodium fast reactor," *Nuclear Engineering and Technology*, vol. 51, no. 3, pp. 665–675, 2019.
- [6] A. Obabko, E. Merzari, L. Brockmeyer et al., "Validation of NEK5000 for 37- and 61-pin wire-wrap geometries with conjugate heat transfer," in *18th International Topical Meeting on Nuclear Reactor Thermal Hydraulics (NURETH)*, pp. 2036–2049, Portland, United States, 2019.
- [7] JAEA, *Sodium technology handbook*, JNC TN9410 2005-011, 2005.
- [8] J.-H. Jeong, J. Yoo, K.-L. Lee, and K.-S. Ha, "Three-dimensional flow phenomena in a wire-wrapped 37-pin fuel bundle for SFR," *Nuclear Engineering and Technology*, vol. 47, no. 5, pp. 523–533, 2015.
- [9] J.-H. Jeong, M.-S. Song, and K.-L. Lee, "CFD investigation of three-dimensional flow phenomena in a JAEA 127-pin wire-wrapped fuel assembly," *Nuclear Engineering and Design*, vol. 323, pp. 166–184, 2017.
- [10] K. Rehme, "Pressure drop correlations for fuel element spacers," *Nuclear Technology*, vol. 17, no. 1, pp. 15–23, 1973.
- [11] F. C. Engel, R. A. Markley, and A. A. Bishop, "Laminar, transition and turbulent parallel flow pressure drop across wire-wrap-spaced rod bundles," *Nuclear Science and Engineering*, vol. 69, no. 2, pp. 290–296, 1979.
- [12] S. K. Cheng and N. E. Todreas, "Hydrodynamic models and correlations for bare and wire-wrapped hexagonal rod bundles – bundle friction factors, subchannel friction factors and mixing parameters," *Nuclear Engineering and Design*, vol. 92, no. 2, pp. 227–251, 1986.

- [13] S. K. Cheng, Y. M. Chen, and N. E. Todreas, "The upgraded Cheng and Todreas correlation for pressure drop in hexagonal wire-wrapped rod bundles," *Nuclear Engineering and Design*, vol. 335, pp. 356–373, 2018.
- [14] S. Rolfo, C. Péniguel, M. Guillaud, and D. Laurence, "Thermal-hydraulic study of a wire spacer fuel assembly," *Nuclear Engineering and Design*, vol. 243, pp. 251–262, 2012.
- [15] O. Bovati, M. A. Yildiz, Y. Hassan, and R. Vaghetto, "RANS simulations for transition and turbulent flow regimes in wire-wrapped rod bundles," *International Journal of Heat and Fluid Flow*, vol. 90, article 108838, 2021.
- [16] Siemens, *Simcenter STAR-CCM+2210 user guide 17.06.007*, Siemens, 2022.
- [17] M. Song, J.-H. Jeong, and E. S. Kim, "Investigation on sub-channel flow distribution in wire-wrapped 37 and 61-pin bundle using computational fluid dynamics," *Nuclear Engineering and Design*, vol. 370, article 110904, 2020.
- [18] A. Shams, A. De Santis, L. K. Koloszar, A. Villa Ortiz, and C. Narayanan, "Status and perspectives of turbulent heat transfer modelling in low-Prandtl number fluids," *Nuclear Engineering and Design*, vol. 353, article 110220, 2019.
- [19] L. Briceux, M. Duponcheel, G. Winckelmans, I. Tiselj, and Y. Bartosiewicz, "Direct and large eddy simulation of turbulent heat transfer at very low Prandtl number: application to lead-bismuth flows," *Nuclear Engineering and Design*, vol. 246, pp. 91–97, 2012.
- [20] A. J. Reynolds, "Расчет турбулентных чисел прандтля и шмидта," *International Journal of Heat and Mass Transfer*, vol. 18, no. 9, pp. 1055–1069, 1975.
- [21] C. David, "Reassessment of the scale-determining equation for advanced turbulence models," *AIAA Journal*, vol. 26, no. 11, pp. 1299–1310, 1988.
- [22] G. Kennedy, K. Van Tichelen, J. Pacio, I. Di Piazza, and H. Uitslag-Doolaard, "Thermal-hydraulic experimental testing of the Myrrha wire-wrapped fuel assembly," *Nuclear Technology*, vol. 206, pp. 179–190, 2020.
- [23] J. Pacio, M. Daubner, T. Wetzel et al., "Experimental nusselt number in rod bundles cooled by heavy-liquid metals," in *Proc. 26th Int Conf. Nuclear Engineering (ICONE26), ICONE26-82213*, ASME, London, England, 2018.
- [24] K. Mikityuk, "Heat transfer to liquid metal: review of data and correlations for tube bundles," *Nuclear Engineering and Design*, vol. 239, no. 4, pp. 680–687, 2009.
- [25] P. A. Ushakov, A. V. Zhukov, and M. M. Matyukhin, "Heat transfer to liquid metals in regular arrays of fuel elements," *High Temperature*, vol. 15, no. 5, pp. 868–873, 1977.
- [26] H. Gräber and M. Rieger, "Experimental study of heat transfer to liquid metals flowing in-line through tube bundles," *Progress in Heat and Mass Transfer*, vol. 7, pp. 151–166, 1973.
- [27] F. Roelofs, V. R. Gopala, S. Jayaraju, A. Shams, and E. Komen, "Review of fuel assembly and pool thermal hydraulics for fast reactors," *Nuclear Engineering and Design*, vol. 265, pp. 1205–1222, 2013.
- [28] OECD-NEA, *Handbook on lead-bismuth eutectic alloy and lead properties, materials compatibility, thermal-hydraulics and technologies*, OECD/NEA Nuclear Science Committee Working Party on Scientific Issues of the Fuel Cycle Working Group on Lead-bismuth Eutectic, 2007.
- [29] K. Yamaguchi, T. Isozaki, and T. Aoki, *Sodium boiling experiments at decay power levels (4)*, Power Reactor and Nuclear Fuel Development Corporation, PNC TN941 85-56, 1985.
- [30] M. H. Fontana, R. E. MacPherson, P. A. Gnadt, L. F. Parsly, and J. L. Wantland, *Temperature distribution in a 19-rod simulated lmfbr fuel assembly in a hexagonal duct (fuel failure mockup bundle 2A)-record of experimental data*, ORNL Reactor Division, ORNL-TM-4113, 1973.
- [31] F. Namekawa, A. Ito, and K. Mawatari, *Buoyancy effects on wire-wrapped rod bundle heat transfer in an LMFBR fuel assembly*, Toshiba Corporation, 1984.
- [32] F. C. Engel, B. Minushkin, R. J. Atkins, and R. A. Markley, "Characterization of heat transfer and temperature distributions in an electrically heated model of an LMFBR blanket assembly," *Nuclear Engineering and Design*, vol. 62, no. 1-3, pp. 335–347, 1980.
- [33] M. Song, J.-H. Jeong, and E. S. Kim, "Flow visualization on SFR wire-wrapped 19-pin bundle geometry using MIR-PIV- PLIF and comparisons with RANS-based CFD analysis," *Annals of Nuclear Energy*, vol. 147, article 107653, 2020.
- [34] K. Dong, S. Ahmad, S. A. Khan, P. Ding, W. Li, and J. Zhao, "Thermal-hydraulic analysis of wire-wrapped rod bundle in lead-based fast reactor with non-uniform heat flux," *International Journal of Energy Research*, vol. 46, no. 12, pp. 16538–16549, 2022.